Microbiota diurnal rhythmicity programs host transcriptome oscillations

Christoph A. Thaiss[1,*], Maayan Levy[1,*], Tal Korem[2,3,*], Lenka Dohnalová[1], Hagit Shaprio[1], Diego A. Jaitin[1], Eyal David[1], Deborah R. Winter[1], Meital Gury-BenAri[1], Evgeny Tatirovsky[1], Timur Tuganbaev[1], Sara Federici[1], Niv Zmora[1], David Zeevi[2,3], Mally Dori-Bachash[1], Meirav Pevsner-Fischer[1], Elena Kartvelishvily[4], Alexander Brandis[5], Alon Harmelin[6], Oren Shibolet[7-9], Zamir Halpern[7-9], Kenya Honda[10,11], Ido Amit[1], Eran Segal[2,3,#], Eran Elinav[1,12,#]

[1]Department of Immunology

[2]Department of Computer Science and Applied Mathematics

[3]Department of Molecular Cell Biology

[4]Electron Microscopy Unit

[5]Targeted Metabolomics Unit, Life Sciences Core Facilities

[6]Department of Veterinary Resources, Weizmann Institute of Science, Rehovot 7610001, Israel

[7]Sackler Faculty of Medicine

[8]Research Center for Digestive Tract and Liver Diseases, Tel Aviv Sourasky Medical Center, Sackler Faculty of Medicine, Tel Aviv University, Tel Aviv 6423906, Israel

[9]Digestive Center, Tel Aviv Sourasky Medical Center, Tel Aviv 6423906, Israel

[10]RIKEN Center for Integrative Medical Sciences (IMS), 1-7-22 Suehiro-cho, Tsurumi-ku, Yokohama, Kanagawa 230-0045, Japan

[11]Department of Microbiology and Immunology, Keio University School of Medicine, 35 Shinanomachi, Shinjuku-ku, Tokyo 160-8582, Japan

[12]Lead contact

*,[#] These authors contributed equally to this work

[#]Correspondence to:

Eran Segal, Ph.D.
Department of Computer Science and Applied Mathematics
Weizmann Institute of Science
Rehovot, Israel 76100
eran.segal@weizmann.ac.il

Eran Elinav, M.D., Ph.D.
Department of Immunology

Weizmann Institute of Science,
100 Herzl Street,
Rehovot, Israel 76100
eran.elinav@weizmann.ac.il

Abstract

The intestinal microbiota undergoes diurnal compositional and functional oscillations that affect metabolic homeostasis, but the mechanisms by which the rhythmic microbiota influences host circadian activity remain elusive. Using integrated multi-omics and imaging approaches, we demonstrate that the gut microbiota features oscillating biogeographical localization and metabolome patterns that determine the rhythmic exposure of the intestinal epithelium to different bacterial species and their metabolites over the course of a day. This diurnal microbial behavior drives, in turn, the global programming of the host circadian transcriptional, epigenetic, and metabolite oscillations. Surprisingly, disruption of homeostatic microbiome rhythmicity not only abrogates normal chromatin and transcriptional oscillations of the host, but also incites genome-wide *de novo* oscillations in both intestine and liver, thereby impacting diurnal fluctuations of host physiology and disease susceptibility. As such, the rhythmic biogeography and metabolome of the intestinal microbiota regulates the temporal organization and functional outcome of host transcriptional and epigenetic programs.

Introduction

The mammalian circadian clock adjusts physiological processes to diurnal environmental variations through the coordination of transcriptome oscillations in peripheral tissues. In each individual cell, the rhythmic transcriptional program is carried out by a network of core clock transcription factors, including period (*Per*), cryptochrome (*Cry*), Bmal (*Arntl*), and Clock, with nuclear receptors of the ROR and REV-ERB families stabilizing the core oscillator (Panda and Hogenesch, 2004). These factors control rhythmic chromatin dynamics, including rhythmic changes in epigenetic marks at circadian promoters, spatial chromosome arrangement, and polymerase activity, thereby determining the fraction of the genome undergoing oscillating expression in a tissue-specific manner (Aguilar-Arnal et al., 2013; Koike et al., 2012; Perelis et al., 2015; Vollmers et al., 2012). As a result, up to 20 percent of a tissue's total transcriptome and up to 50 percent of all transcripts in the body consist of oscillating elements, which determine the diurnal pattern of cellular and organismal activity (Panda et al., 2002; Zhang et al., 2014).

Cellular metabolism is greatly affected by the activity of the circadian clock, thereby accomodating the temporal variation of an organism's metabolic needs over the course of a day. For instance, the rhythmic fluctuations of metabolite levels in a given tissue are driven by the components of the molecular clock (Adamovich et al., 2014; Dallmann et al., 2012; Eckel-Mahan et al., 2012; Minami et al., 2009). In turn, metabolic products serve as an important input into the circadian clock network, thereby creating a bi-directional feedback loop of reciprocal control between cellular metabolic activity and the circadian clock (Asher et al., 2008; Nakahata et al., 2008; Nakahata et al., 2009; Ramsey et al., 2009; Zwighaft et al., 2015).

In addition to the circadian variation in the physiology of the host, it was recently discovered that the community of bacteria colonizing the mammalian gastrointestinal tract, collectively called the intestinal microbiota, undergoes diurnal oscillations in composition and function (Leone et al., 2015; Liang et al., 2015; Thaiss et al., 2014; Zarrinpar et al., 2014). These oscillations are controlled by the timing of food intake and the composition of the diet (Leone et al., 2015; Thaiss et al., 2015a; Zarrinpar et al., 2014). The diurnal interaction between the host and its gut microbiome can affect circadian clock activity in different tissues (Leone et al., 2015; Mukherji et al., 2013; Murakami et al., 2016) and is particularly critical for metabolic homeostasis of the host, as failure to rhythmically control the microbiota results in dysbiosis that promotes obesity and other manifestations of the metabolic syndrome (Thaiss et al., 2015b; Voigt et al., 2014; Voigt et al., 2016). However, how the rhythmic activity of the microbiota feeds into the circadian clock network both locally in the intestine and systemically, and how this concerted host-microbiome oscillation impacts diurnal organ physiology remains elusive.

In this study, we performed a system-wide analysis of the daily host-microbiota interplay in order to determine the functional properties of microbiota oscillations that impact the circadian activity of the host. We find that the biogeography and metabolome of the intestinal microbiota, two features that substantially influence host physiology, undergo diurnal oscillations. Abrogation of these rhythms by antibiotic treatment or in germ-free mice leads to a massive reprogramming of the epigenetic and transcriptional landscape in the intestine, including a large-scale *de novo* generation of oscillating histone marks and rhythmically expressed genes. Furthermore, the microbiota metabolome influences rhythmic host physiology beyond the intestine, by driving systemic metabolite rhythms and programming of transcriptional oscillations in the liver. Thereby, the microbiota impacts the homeostatic diurnal variation in hepatic drug detoxification and hepatotoxicity. Together, this work identifies several new layers of diurnality at the host-microbiota interface, implicates the microbiome as a major source of clock-modifying metabolites, and suggests the microbiome as a regulator of host circadian activity.

Results

The biogeography of the intestinal microbiota undergoes diurnal oscillations

Since the commensal bacteria most strongly affecting the host are located in proximity to the intestinal mucosal surface, we studied the biogeographical aspects of microbiome diurnal rhythmicity, by analyzing fluctuations in the abundance, composition, and function of epithelial-adherent commensal bacteria in the colon over the course of two days (**Figure 1A**). All mice were fed ad libitum and housed under strict 24-hour dark-light conditions, with lights being kept on for 12 hours (Zeitgeber times (ZT) 0-12). Scanning electron microscopy (SEM) imaging of proximal colons revealed daily fluctuations in the amount of commensals in tight association with the intestinal epithelium (**Figures 1B, S1A,** and **S1B**, $p<10^{-5}$, JTK_cycle). To determine the absolute numbers of mucosal-associated bacteria, we extensively cleared proximal colons from luminal content to retain only the mucosal niche, and confirmed the successful isolation of epithelial-proximal bacteria by detection of mucus-resident commensals, including *Mucispirillum schaedleri* (Robertson et al., 2005). In line with the observations made by SEM, the numbers of bacteria colonizing the epithelial niche, as quantified by qPCR of the total 16s rDNA pool, underwent marked diurnal changes, with epithelial layer adherence in the dark phase being up to 10-fold higher than in the light phase (**Figure 1C**, $p<10^{-6}$). We confirmed these results by using a sampling frequency of 4 hours (**Figure S1C**). To assess whether the bacterial composition in the mucosal niche likewise underwent temporal fluctuations, we performed 16S rDNA sequencing of epithelial-associated communities harvested at different times of the day. Indeed, the global bacterial

composition featured marked diurnal oscillations (**Figures 1D** and **1E)**, such that the bacterial community localized to the intestinal mucosa at any time point was more similar to the one present 24 hours earlier than to any other time point in between (**Figures S1D-S1F**). To determine the absolute numbers of bacteria colonizing the mucosal niche we then combined 16S sequencing with qPCR quantification (**Figure S1G**). 148 out of 633 detected operational taxonomic units (OTUs) featured rhythmic patterns of epithelial adherence (**Figure 1F**, $p<0.05$, $q<0.1$), including *Mucispirillum schaedleri* (**Figure 1G**), *Lactobacillus reuteri* (**Figure S1H**), and *Bacteroides acidifaciens* (**Figure S1I**). Together, these results suggest that the host mucosa is exposed to diurnally fluctuating numbers and species of bacteria over the course of a day.

Host and microbial factors regulate bacterial mucosal-associated oscillations

To determine the mechanisms driving rhythmic bacterial mucosal localization, we performed metagenomic sequencing of the mucosal microbial community every 6 hours over the course of 48 hours. We first assessed rhythmic changes in the abundance of bacterial KEGG genes in epithelial proximity. 404 out of 1552 genes significantly oscillated in their relative abundances, among them members of the flagellar gene operons (**Figures 1H and 1I**, $p<0.05$, $q<0.1$). We furthermore assigned KEGG modules and pathways to the microbial genes (**Figures 2A** and **S2A**). Interestingly we found pathways involved in mucus degradation (**Figures 1H, 2A,** and **S2A**) and bacterial motility (**Figures 1H, 2A,** and **S2A**) to be among the microbial functions most significantly oscillating in relative abundance, as exemplified by bacterial chemotaxis (**Figure 2B**) and flagellar assembly (**Figure S2B**). To determine the bacterial species driving pathway-level rhythmicity in the mucosal community, we examined those OTUs that contributed to oscillating genes within the bacterial chemotaxis and flagellar assembly pathways. Notably, the majority of such species belonged to *Deferribacteraceae* (**Tables S1 and S2**), a bacterial family which itself featured robust oscillations in mucosal abundance (**Figure S2C**).

We hypothesized that rhythmic bacterial movement and mucus invasion might contribute to the daily fluctuations in commensal inhabitation of the mucosal niche. We therefore performed a time course of microbiota imaging by 16S *in situ* hybridization every 6 hours over the course of two days, using a mucus-preserving fixation method and co-staining for Muc2 protein in order to visualize mucus production. Expectedly, we found a two-layered mucus structure, the inner of which is largely free of bacterial colonization (**Figure S2D**). Interestingly, the thickness of the mucus layer, as well as the degree of microbial penetration into the mucus layer and thus the width of spatial separation between the host intestinal epithelium and the commensal bacteria, underwent rhythmic fluctuations (**Figures**

2C, 2D, and **S2D**). Microbial proximity to the mucosal surface was highest during the dark phase (**Figure 2C**, $p<10^{-20}$), corroborating the results obtained by electron microscopy and 16S qPCR.

The spatial segregation between epithelial layer and commensal bacteria is maintained by the production of mucus and antimicrobial peptides (Hooper et al., 2012; Johansson et al., 2008; Vaishnava et al., 2011; Wlodarska et al., 2014). Recently, it was found that mice lacking RegIIIγ feature enhanced bacterial colonization in direct proximity to the intestinal epithelium (Loonen et al., 2014; Vaishnava et al., 2011). Indeed, we found an impairment of spatial separation between the epithelial layer and the microbiota and abrogated diurnal rhythmicity in the number of mucosal-resident bacteria in RegIIIγ-deficient mice, as determined by in-situ hybridization (**Figures 2E** and **S2E**), 16S qPCR (**Figure 2F**), and 16S sequencing (**Figure S2F**).

To determine the contribution of the host circadian machinery to the circadian bacterial adherence patterns, we utilized *Per1/2*$^{-/-}$ mice that are devoid of the core molecular clock (Adamovich et al., 2014). We noted a marked loss of bacterial adherence oscillations in *Per1/2*$^{-/-}$ mice, (**Figure 2G**), indicating that host circadian rhythms are indispensable for the maintenance of microbiota biogeographical rhythms. To disentangle the dysfunctional molecular clock from abrogated feeding rhythms noted in these mice (Neufeld-Cohen et al., 2016), we performed timed-feeding experiments, in which *Per1/2*$^{-/-}$ mice had access to food only during the light phase. Notably, this treatment restored microbiota oscillations, both in the amount and composition of the mucosal-resident bacterial community (**Figures 2H, 2I, S2G,** and **S2H**). These results identify feeding time as a major driver of microbial biogeography. In support of this notion, wild-type mice that were fed either only during the dark or only during the light period showed phase-reversed microbial attachment rhythms (**Figure S2I**).

Together, these results identified several host and microbial factors jointly contributing to diurnal variations in epithelial proximity of commensal bacteria, including the host circadian clock through regulation of feeding rhythms, RegIIIγ-mediated barrier function, as well as rhythmic bacterial motility and mucus degradation.

Microbiota ablation reprograms the intestinal circadian transcriptome

We next assessed the impact of the diurnally fluctuating microbiome on the intestinal epithelium. To this end, we disrupted the bacterial ecosystem by administering broad-spectrum antibiotics and assessed the host circadian transcriptional and epigenetic intestinal program (**Figure 3A**). Expectedly, antibiotic treatment abrogated both the number of mucosal-associated bacteria and their oscillatory behavior, as determined by 16S qPCR and scanning electron microscopy (**Figures 3B, 3C,** and **S3A**).

Furthermore, the remaining antibiotic-persistent epithelial-proximal microbiota lost its diurnal rhythms in composition (**Figures 3D, 3E, S3B,** and **S3C**).

To determine the impact of microbiota disruption on the rhythmic transcriptome of the host, we performed comparative RNA-sequencing of colonic tissue from control and antibiotics-treated mice every 6 hours over the course of two light-dark cycles (**Figure 3A**). We first confirmed the detection of known effects of microbiota depletion on colonic transcription by qPCR (**Figure S3D**). We next evaluated host transcript rhythmicity on a global level. Interestingly, while robust circadian oscillations were detected in several hundred genes in both control and antibiotics-treated groups, the identity of the most significantly oscillating genes was markedly different between the groups, which was observed with both 6 hours and 4 hours sampling frequency (**Figures 3F-3I** and **S3E**). Behavioral rhythms of the host, including feeding rhythmicity, persisted throughout the antibiotic treatment (**Figures S3F, S3G**, and data not shown), ruling out loss of rhythmic food intake as the reason for the observed transcriptional reprogramming. Loss and gain of oscillatory host transcripts was unrelated to expression levels, since average expression of the affected genes was not influenced by antibiotic treatment (**Figure S3H**), suggesting that transcript oscillation was an independently regulated feature.

To determine the functionality of lost, gained, and shared transcript oscillations, we assigned KEGG pathways to each group of genes. The pathway most significantly enriched among the oscillatory transcripts shared between antibiotic treated and control mice was the core circadian clock ($p<10^{-9}$), indicating that the function of the host peripheral clock machinery was not intrinsically dependent on the presence of an intact microbiota (**Figures 3G** and **3J**). Transcripts that lost their oscillations in the absence of the microbiota mainly belonged to nucleotide metabolism and cell cycle pathways (**Figures 3H** and **3K**). Most remarkable and unexpected, however, were the functionalities that gained rhythmicity upon microbiota depletion, which included major metabolic pathways like pyruvate metabolism, glutathione metabolism, and the TCA cycle (**Figures 3I** and **3L**). Interestingly, similar pathways were significantly oscillating in the mucosal microbiome under homeostatic conditions (**Figure S3I**), potentially suggesting that upon microbiota depletion, the host may acquire compensatory oscillatory programs in functionalities that are normally performed by the microbiota in a rhythmic manner. These data indicate that a large set of rhythmic transcripts in the colon is influenced by the intestinal microbiota, and that microbiota depletion incites *de novo* oscillatory programs in the host.

Microbiota ablation reprograms circadian chromatin dynamics

To gain insight into the mechanisms by which the microbiota influences the programming of colonic transcriptome oscillations, we investigated the gene regulatory mechanisms underlying rhythmic transcription in intestinal epithelial cells. Clock-driven transcriptome oscillations in the liver are accompanied by rhythmic genome-wide remodeling of the chromatin state (Koike et al., 2012; Vollmers et al., 2012). We therefore sought to characterize the circadian epigenetic landscape of intestinal epithelial cells, and to determine whether the microbiota influences rhythmic chromatin remodeling in a genome-wide manner. To this end, we performed a time-course of chromatin immunoprecipitation followed by next-generation sequencing (ChIP-seq) profiling on purified intestinal epithelial cells every 6 hours over two days (**Figure 4A**). We assayed several histone modifications including trimethylation of histone H3 at lysine 4 (H3K4me3), H3K4me2, and H3K27 acetylation (H3K27ac) to determine the global landscape of enhancers (distal regions marked by H3K4me2), promoters (characterized by the enrichment of H3K4me3) and active transcription, indicated by H3K27Ac marks (**Figure 4A**).

Given the close association of circadian promoters and rhythmic transcription (Koike et al., 2012; Vollmers et al., 2012), we first examined the genome-wide architecture of active promoters. To this end, we identified H3K27ac peaks in H3K4me3 regions and assessed rhythmicity over the course of two days by JTK_cycle. We found significant oscillations in 525 active promoters (**Figure S4A**, $p<0.05$), including the loci of the canonical clock genes (**Figure S4B**). We ruled out false-positive detection of stochastic oscillations by comparing rhythmic histone marks to the genomic background of whole-cell extracts (**Figure S4A**). Using this map of genome-wide oscillations in active promoters, we next addressed the impact of the microbiome on the temporal organization of the chromatin landscape, by performing a ChIP-seq time-course on antibiotics-treated mice (**Figure 4A**). Remarkably, and in agreement with the gene expression data, we found cycling behavior of promoter marks in both control and antibiotics groups, but the identity of the oscillating loci was largely distinct (**Figures 4B** and **4C**), with 491 promoters losing rhythmicity upon microbiota depletion, but 477 loci developing *de novo* rhythmic behavior (**Figure 4C**). Among the genes with shared promoter rhythmicity were genes associated with the core clock, as exemplified by *Dbp* (**Figures 4D** and **S4C**), while the loss and gain of oscillations affected genes across various functional groups (**Figures 4E** and **4F**). The examples of *Nr1d1* (shared oscillation), *Mxd1* (lost oscillation), and *Cxadr* (*de novo* oscillation) illustrate the association of loss and gain of H3K27ac rhythmicity at promoter regions with transcript oscillations (**Figure S4D**).

In addition to active promoters, circadian transcription is closely associated with cyclic enhancer regions (Koike et al., 2012; Vollmers et al., 2012). We therefore also focused on rhythmic H3K4me2 peaks and investigated the impact of the microbiota on the diurnal enhancer landscape. As with circadian promoters, overall rhythmicity was not affected by microbiota depletion (**Figures 4G** and

S4E). However, the loci of both rhythmic enhancer usage (H3K4me2) and enhancer activity (H3K4me2 + H3K27ac) substantially differed between both scenarios, with several hundreds of enhancers losing and gaining rhythmicity upon antibiotic treatment (**Figures 4H** and **S4F**). When we examined active enhancers (H3K27ac oscillations at intergenic and intragenic H3K4me2 loci), we observed a strong association of cycling genes with cycling enhancer marks in the antibiotics setting, suggesting that the rhythmic behavior of such enhancers becomes active upon changes in the state of microbial colonization. Such enhancer activity-driven *de novo* oscillation was observed, for example, in the calcium-binding protein *S100a10* (**Figures 4I** and **4J**), while loss of rhythmicity is exemplified by the phosphatase *Ctdsp2* (**Figures 4K** and **4L**). Malate dehydrogenase (*Mdh1*) represented a further example in which enhancer activity (H3K4me2 + H3K27ac), rather than enhancer usage (H3K4me2 alone), regulated the activation of oscillating transcription upon microbiota depletion (**Figures S4G** and **S4H**). Together, these data demonstrate an impact of the microbiota on the architecture of oscillating chromatin modifications and suggest that microbial colonization influences rhythmic promoter and enhancer activity to drive rhythmic gene expression.

Microbial attachment influences the intestinal circadian transcriptome

The above antibiotic treatment experiments suggested that the microbiome regulates oscillations in the host transcriptome and epigenome, but could not distinguish between the involvement of bacterial attachment to the mucosa or its mere presence in the intestine. To differentiate between these two possibilities, we mono-colonized germ-free mice with adherent and non-adherent variants of the same bacterial species (**Figure 5A**). We used segmented filamentous bacteria (SFB) indigenous to mice (mSFB) or rats (rSFB), previously shown to feature differential adherence to the intestinal epithelium (Atarashi et al., 2015). Indeed, mSFB was found in more than 10-fold higher numbers in the mucosal-proximal layer of mice as compared to rSFB (**Figure 5B**). Despite these differences in mucosal colonization, both types of SFB featured phase-shifted rhythmic patterns of absolute numbers in epithelial proximity over the course of 48 hours (**Figure 5C**).

This system enabled us to determine the impact of differential rhythmic bacterial attachment of the colonic circadian transcriptome in mice mono-colonized with mSFB (featuring a rhythmic mucosal abundance), mice mono-colonized with rSFB (featuring a rhythmic yet markedly reduced mucosal abundance), and mice lacking RegIIIγ (featuring an abundant but non-rhythmic mucosal microbiome, **Figure 2F**). We compared the identity of oscillating genes in these mice with those featured in either antibiotics-treated or control mice (**Figure 3F**). Notably, the oscillating transcripts of mSFB-mono-colonized mice were most similar to wild-type controls (**Figure 5D**) while those of *Reg3g*$^{-/-}$ mice showed

the strongest overlap with those of antibiotics-treated animals, suggesting that rhythmic bacterial adherence per se was involved in determining the program of rhythmically expressed genes. Mono-colonization with rSFB resulted in an intermediate oscillatory program, possibly reflecting its combination of reduced adherence yet oscillating microbiome activity (**Figure 5D**). These alterations in rhythmic transcription did not influence oscillations of the core molecular clock, as exemplified by *Dbp* expression (**Figure 5E**). Apart from the members of the circadian clock, mSFB mono-colonization was associated with rhythmic transcription of genes belonging to DNA replication, cell cycle, and nucleotide turnover pathways (**Figure 5F**), similar to control mice harboring a conventional microbiome (**Figure 3K**). Together, these results suggest that rhythmic bacterial adherence drives a program of transcriptional oscillations that is altered upon interference with the rhythmic biogeography of the microbiota.

Microbiota ablation reprograms the hepatic circadian transcriptome

We next examined whether the impact of the microbiota on oscillatory programs of the host reaches beyond the gastrointestinal tract. To this end, we performed RNA-seq analysis of livers from antibiotics-treated or control mice taken at 6 hour intervals over two days and assessed for rhythmicity using JTK_cycle (**Figure 5G**). Similar to what we had observed in the colon, antibiotics-mediated microbiota disruption reprogrammed liver transcriptome oscillations (**Figures 5H** and **S5A-C**), without changing the mean expression levels of the affected genes (**Figure S5D**). As in the gut, the canonical clock components maintained their rhythms (**Figures 5I, 5J, S5A,** and **S5E**), as did genes involved in hepatic drug metabolism, insulin signaling, and multiple other metabolic functions (**Figures 5I** and **S5A**). In total, 375 out of 1306 hepatic transcripts cycled only in the control group ($p<0.05$, $q<0.1$; **Figure 5H**), including genes involved in oxidative phosphorylation and other catabolic pathways (**Figures 5K** and **S5B**). For instance, the gene encoding glucose phosphate isomerase-1 (*Gpi1*) lost detectable rhythmicity after antibiotic treatment (**Figure 5K**). In contrast, 912 transcripts developed *de novo* rhythmicity ($p<0.05$, $q<0.1$; **Figures 5H** and **S5C**), many of which were involved in amino acid metabolism and fatty acid metabolism, including elements of the PPARγ signaling pathway (**Figures 5L**) (Murakami et al., 2016). To corroborate that this transcriptional reprogramming was due to microbiota depletion, rather than direct effects of the antibiotics on the liver, we profiled the circadian hepatic transcriptome of germ-free mice and compared the results to the profile found in colonized control mice and mice treated with broad-spectrum antibiotics. We found a high concordance of oscillating transcripts in livers from germ-free mice with those from antibiotics-treated mice, while the overlap with non-treated control mice was smaller (**Figure S5F**). Taken together, these results highlight the microbiota as being critical for maintaining the homeostatic rhythmic transcription in the liver.

The microbiota programs the hepatic transcriptome through systemic metabolome oscillations

We next sought to determine the mechanisms by which the gut microbiota distally orchestrates hepatic transcriptome oscillations. Metabolism has emerged as a major regulator of the epigenetic control of gene expression, and several prominent examples of close interaction between metabolites and the circadian clock have been unraveled (Asher and Sassone-Corsi, 2015). To gain insight into metabolites as potential mediators of the effect that the microbiota exerts on rhythmic gene expression, we first determined the temporal dynamics of the intestinal metabolome by metabolomic profiling in wild-type mice every 6 hours over the course of two light-dark cycles (**Figure 5G**). We detected significant oscillations across diverse chemical groups, including lipids, amino acids, carbohydrates, vitamins, nucleotides, and xenobiotics (**Figures 6A**), as exemplified by the carbohydrate xylose, the dipeptide valylglutamate, and the histidine derivative ergothioneine (**Figures S6A-C**). Oscillatory behavior was detected along biosynthetic pathways, such as the conversion between the polyamine ornithine and the amino acid proline (**Figure 6B,** $p<10^{-3}$). In the case of biotin, a bacterial-derived vitamin with essential functions for host physiology, we noted rhythmicity along the biosynthetic pathway (**Figure 6C,** $p<10^{-5}$), involving the conversion of 7,8-diaminononanoate to dethiobiotin (catalyzed by bioD), and the subsequent production of biotin (catalyzed by bioB). Furthermore, rhythmic elements characterized the glycolytic conversion of sucrose to lactate (**Figure S6D**). These results demonstrate that multiple microbiota-derived and -modulated metabolites undergo diurnal rhythms, suggesting a potential mechanism by which microbiota metabolism may influence the diurnal transcriptional landscape of the host.

To determine interactions between oscillating intestinal metabolites and systemic host circadian activity, we profiled the temporal behavior of serum metabolites over a 48-hour time course (**Figure 5G**). We focused on amino acids and polyamines, given their prominent rhythmicity in the lumen of the gastrointestinal tract and their known regulatory involvement in the activity of the circadian clock (Zwighaft et al., 2015). Notably, we found a high degree of concordance between rhythmicity of a particular metabolite in the serum and in the intestinal lumen ($R^2=0.415$, $p<10^{-3}$; **Figure 6D**). Some metabolites featured phase-shifted oscillations in the serum, as demonstrated for threonine, ornithine, proline, and α-aminobutyric acid (**Figures 6E** and **S6E-S6G**). To test whether the microbiota was involved in the orchestration of this serum rhythmicity of amino acids and polyamines, we profiled their diurnal pattern in antibiotics-treated and germ-free mice. Remarkably, absence of the microbiota abolished rhythmicity in any of the examined metabolites (**Figure 6F**). For instance, antibiotics-treated and germ-free mice did not show diurnal rhythms in the serum levels of ornithine (**Figures 6G** and **6H**). Furthermore, while arrhythmic *Per1/2*$^{-/-}$ mice did not feature any detectable serum amino acid or

polyamine oscillations, restoring microbiota oscillations in these mice by timed feeding reinstated metabolite rhythms to the level of wild-type controls (**Figures 6F** and **S6H**). This was seen, for instance, in ornithine and the biosynthetically related metabolites arginine and proline (**Figures 6I, S6I,** and **S6J**).

To further investigate whether the levels and fluctuations of intestinal amino acids and polyamines were causally involved in the reprogramming of hepatic transcript oscillations, we performed a dietary intervention in which mice were fed a polyamine-deficient (PD) diet for 4 weeks, followed by serum metabolite analysis and RNA-seq of hepatic tissue every 6 hours over two days (**Figure 7A**). Indeed, PD diet abrogated homeostatic circadian oscillations in serum amino acids and polyamines (**Figures 7B** and **S7A-S7C**). Remarkably, this was accompanied by reprogramming of the hepatic circadian transcriptome, including the loss and de-novo gain of several hundreds of rhythmic genes (**Figures 7C-7G**). The genes oscillating in mice fed a PD diet showed the highest concordance with those measured in antibiotics-treated mice, and to a much lesser extent to non-treated control mice (**Figure 7D**). Together, these results suggest that diet and the gut microbiota are central contributors to the maintenance of systemic metabolome rhythms, thereby impacting the programming of the circadian hepatic transcriptome. In demonstrating these links between diet, microbiome, circulating metabolites, and the liver, we focused as proof-of-concept on amino acids and polyamines, while similar impacts by other metabolite families merit further studies.

Microbiota-mediated reprogramming of the circadian transcriptome alters diurnal hepatic detoxification

Finally, we considered the consequences of microbiota-mediated reprogramming of the daily sequence of gene expression for the physiological function of the liver. The time of day is known to greatly affect hepatic drug metabolism, including the detoxification of acetaminophen (acetyl-para-aminophenol, APAP) (Kim and Lee, 1998). Additionally, the microbiota has been implicated in APAP metabolism (Clayton et al., 2009). We therefore administered APAP at different circadian times (ZT0 versus ZT12) and assessed APAP-induced hepatotoxicity by the measurement of liver enzyme release as well as liver histology. In line with previous reports (Johnson et al., 2014; Kim and Lee, 1998), mice featured dramatically exacerbated liver toxicity when APAP was injected at ZT12 as compared to ZT0 (**Figure 7H-7K**). This diurnal variation was clock-dependent, as *Per1/2*$^{-/-}$ mice did not feature differential hepatotoxicity between ZT 0 and ZT12 (**Figures S7D-S7G**). Remarkably, antibiotics-treated or germ-free mice lost this diurnal variation in the severity of APAP-induced hepatotoxicity, and featured low and comparable levels of liver damage at different times of the day (**Figure 7H-7K**), manifesting as a significantly lower aminotransferase activity, reduced liver necrosis, and improved

histopathological score. Together, these results suggest that homeostatic microbiota rhythms and microbiota-mediated maintenance of the circadian transcriptome is necessary to maintain normal diurnal activity in hepatic drug metabolism.

Discussion

In this study, we profiled the global landscape of diurnal host-microbiota interactions on the level of bacterial biogeography, metagenomic functions, host epigenome, host gene expression, as well as intestinal and serum metabolomes. We found that the bacterial microbiome features rhythmic patterns of localization and metabolite secretion in the large intestine. These rhythms influence diurnal gene expression locally in the intestine and distally in the liver. Surprisingly, ablation of microbiota rhythms by antibiotic treatment and in germ-free mice not only leads to a loss of oscillations on the chromatin and transcript level, but also concomitantly incites a massive gain of *de novo* oscillations, resulting in a temporal reorganization of metabolic pathways in both intestine and liver.

These results have numerous important implications. First, our study identifies diurnal rhythmicity as an essential component in the regulation of host-microbiota symbiosis. While diurnal rhythms have so far been mainly described on the level of bacterial genome abundance (Leone et al., 2015; Liang et al., 2015; Thaiss et al., 2014; Zarrinpar et al., 2014), we highlight two new elements of microbiota oscillatory activity that provide a mechanistic explanation for its functional importance: oscillations in microbiota metabolome and biogeographical localization, inducing a homeostatic state in which the host is periodically exposed to different bacterial numbers, species, functions, and products at different times of the day. If homeostatic colonization is abrogated, as in the case of antibiotic treatment, compositional and biogeographical rhythmicity are lost, ultimately resulting in uncoupling of the corresponding host rhythmicity.

Furthermore, our results support the notion that the circadian program of epigenetic and transcriptional oscillations driven by peripheral clocks is not independent of environmental signals, but integrates these signals into the daily succession of gene regulatory programs. In this study, we identify the microbiome as a critical factor regulating the selection of host genes expressed in a rhythmic manner. Interestingly, we found that members of the core clock and associated genes oscillate independently of microbial influences. Our results therefore suggest a model by which the molecular clock as well as the poised promoter and enhancer regions of a large portion of the genome undergo self-sustained rhythmicity, while the downstream induction of rhythmicity in large portions of the transcriptome depends on the proper interpretation of environmental signals, such as the sensing of fluctuating levels of metabolite abundances. As such, the microbiota can be regarded as an

endogenous “circadian organizer” (Masri et al., 2016), whose signals are integrated by peripheral tissues to affect the temporal organization of genome-wide transcription.

Finally, our study provides insights into the functional consequences of the microbiome-mediated disruption of normal circadian physiology. We show that antibiotic treatment or disruption of circadian feeding behavior leads to a multi-faceted disruption of microbiota diurnal rhythmicity, thereby generating a temporal de-synchronization of circadian liver functions. The metabolism of APAP by both host and microbiota is one such example of a diurnally shifting housekeeping activity, in which the time of exposure to an APAP overdose determines the production level of hepatotoxic APAP degradation products. This diurnal activity, and its functional consequences during APAP intoxication, is abrogated in antibiotic-treated or germ-free mice, highlighting the microbiome as major contributor to the chronopharamcology of drugs, environmental xenobiotics, and dietary components. Together, understanding of the role of the microbiome in the diurnal adaptation of peripheral organ activity may prove instrumental for understanding and treating human conditions associated with disruption of the microbiota and the circadian clock.

Acknowledgements

We thank the members of the Elinav and Segal labs for discussions and Ilan Rosenshine for sharing important tools. We acknowledge Ziv Zwighaft and Gad Asher for providing polyamine-deficient animal diet and helpful advice, and Tevie Mehlman, Carmit Bar-Nathan, Osnat Amram, as well as the Weizmann Histology Unit for technical support. C.A.T. received a Boehringer Ingelheim Fonds PhD Fellowship and thanks Shalev Itzkovitz and Yair Raisner for insightful discussions. T.K. is supported by the Ministry of Science, Technology & Space, Israel. N.Z. is supported by the Gilead Sciences International Research Scholars Program in Liver Disease. K.H. is supported by CREST, Japan Agency for Medical Research and Development. E.S. is supported by the Crown Human Genome Center; the Else Kroener Fresenius Foundation; Donald L. Schwarz, Sherman Oaks, CA; Jack N. Halpern, New York, NY; Leesa Steinberg, Canada; and grants funded by the European Research Council and the Israel Science Foundation. E.E. is supported by Yael and Rami Ungar, Israel; Leona M. and Harry B. Helmsley Charitable Trust; the Gurwin Family Fund for Scientific Research; Crown Endowment Fund for Immunological Research; estate of Jack Gitlitz; estate of Lydia Hershkovich; the Benoziyo Endowment Fund for the Advancement of Science; Adelis Foundation; John L. and Vera Schwartz, Pacific Palisades; Alan Markovitz, Canada; Cynthia Adelson, Canada; CNRS (Centre National de la Recherche Scientifique); estate of Samuel and Alwyn J. Weber; Mr. and Mrs. Donald L. Schwarz, Sherman Oaks; grants funded by the European Research Council; the German-Israel Binational foundation; the Israel Science Foundation; the Minerva Foundation; the Rising Tide foundation; and the Alon Foundation scholar award. E.E. is the incumbent of the Rina Gudinski Career Development Chair and a senior fellow of the Canadian Institute For Advanced Research (CIFAR).

Author Contributions

C.A.T. and M.L. conceived the study, designed, performed and interpreted the experiments, and wrote the manuscript. T.K. developed and performed bioinformatics and statistical analysis. L.D., H.S., D.A.J., M.G-B.., E.T., T.T., S.F., N.Z., M. D.-B. and M. P.-F. helped with experiments. E.D., D.R.W., and D.Z. performed bioinformatics analysis. E.K. performed electron microscopy. A.B. performed metabolite analysis. A.H., O.S., Z.H., and K.H. provided essential tools and insights. I.A. supervised the transcriptomics part of the study. E.S. and E.E. conceived the study, supervised the participants, interpreted the experiments, and wrote the manuscript.

References

Adamovich, Y., Rousso-Noori, L., Zwighaft, Z., Neufeld-Cohen, A., Golik, M., Kraut-Cohen, J., Wang, M., Han, X., and Asher, G. (2014). Circadian clocks and feeding time regulate the oscillations and levels of hepatic triglycerides. Cell metabolism *19*, 319-330.

Aguilar-Arnal, L., Hakim, O., Patel, V.R., Baldi, P., Hager, G.L., and Sassone-Corsi, P. (2013). Cycles in spatial and temporal chromosomal organization driven by the circadian clock. Nature structural & molecular biology *20*, 1206-1213.

Asher, G., Gatfield, D., Stratmann, M., Reinke, H., Dibner, C., Kreppel, F., Mostoslavsky, R., Alt, F.W., and Schibler, U. (2008). SIRT1 regulates circadian clock gene expression through PER2 deacetylation. Cell *134*, 317-328.

Asher, G., and Sassone-Corsi, P. (2015). Time for food: the intimate interplay between nutrition, metabolism, and the circadian clock. Cell *161*, 84-92.

Atarashi, K., Tanoue, T., Ando, M., Kamada, N., Nagano, Y., Narushima, S., Suda, W., Imaoka, A., Setoyama, H., Nagamori, T.*, et al.* (2015). Th17 Cell Induction by Adhesion of Microbes to Intestinal Epithelial Cells. Cell *163*, 367-380.

Bolger, A.M., Lohse, M., and Usadel, B. (2014). Trimmomatic: a flexible trimmer for Illumina sequence data. Bioinformatics *30*, 2114-2120.

Boughton, B.A., Callahan, D.L., Silva, C., Bowne, J., Nahid, A., Rupasinghe, T., Tull, D.L., McConville, M.J., Bacic, A., and Roessner, U. (2011). Comprehensive profiling and quantitation of amine group containing metabolites. Anal Chem *83*, 7523-7530.

Caporaso, J.G., Kuczynski, J., Stombaugh, J., Bittinger, K., Bushman, F.D., Costello, E.K., Fierer, N., Pena, A.G., Goodrich, J.K., Gordon, J.I.*, et al.* (2010). QIIME allows analysis of high-throughput community sequencing data. Nature methods *7*, 335-336.

Clayton, T.A., Baker, D., Lindon, J.C., Everett, J.R., and Nicholson, J.K. (2009). Pharmacometabonomic identification of a significant host-microbiome metabolic interaction affecting human drug metabolism. Proceedings of the National Academy of Sciences of the United States of America *106*, 14728-14733.

Dallmann, R., Viola, A.U., Tarokh, L., Cajochen, C., and Brown, S.A. (2012). The human circadian metabolome. Proceedings of the National Academy of Sciences of the United States of America *109*, 2625-2629.

Dennis, G., Jr., Sherman, B.T., Hosack, D.A., Yang, J., Gao, W., Lane, H.C., and Lempicki, R.A. (2003). DAVID: Database for Annotation, Visualization, and Integrated Discovery. Genome Biol *4*, P3.

Eckel-Mahan, K.L., Patel, V.R., Mohney, R.P., Vignola, K.S., Baldi, P., and Sassone-Corsi, P. (2012). Coordination of the transcriptome and metabolome by the circadian clock. Proceedings of the National Academy of Sciences of the United States of America *109*, 5541-5546.

Gury-BenAri, M., Thaiss, C.A., Serafini, N., Winter, D.R., Giladi, A., Lara-Astiaso, D., Levy, M., Salame, T.M., Weiner, A., David, E.*, et al.* (2016). The Spectrum and Regulatory Landscape of Intestinal Innate Lymphoid Cells Are Shaped by the Microbiome. Cell *166*, 1231-1246 e1213.

Heinz, S., Benner, C., Spann, N., Bertolino, E., Lin, Y.C., Laslo, P., Cheng, J.X., Murre, C., Singh, H., and Glass, C.K. (2010). Simple combinations of lineage-determining transcription factors prime cis-regulatory elements required for macrophage and B cell identities. Mol Cell *38*, 576-589.

Hooper, L.V., Littman, D.R., and Macpherson, A.J. (2012). Interactions between the microbiota and the immune system. Science *336*, 1268-1273.

Hughes, M.E., Hogenesch, J.B., and Kornacker, K. (2010). JTK_CYCLE: an efficient nonparametric algorithm for detecting rhythmic components in genome-scale data sets. Journal of biological rhythms *25*, 372-380.

Jaitin, D.A., Kenigsberg, E., Keren-Shaul, H., Elefant, N., Paul, F., Zaretsky, I., Mildner, A., Cohen, N., Jung, S., Tanay, A.*, et al.* (2014). Massively parallel single-cell RNA-seq for marker-free decomposition of tissues into cell types. Science *343*, 776-779.

Johansson, M.E., Phillipson, M., Petersson, J., Velcich, A., Holm, L., and Hansson, G.C. (2008). The inner of the two Muc2 mucin-dependent mucus layers in colon is devoid of bacteria. Proceedings of the National Academy of Sciences of the United States of America *105*, 15064-15069.
Johnson, B.P., Walisser, J.A., Liu, Y., Shen, A.L., McDearmon, E.L., Moran, S.M., McIntosh, B.E., Vollrath, A.L., Schook, A.C., Takahashi, J.S.*, et al.* (2014). Hepatocyte circadian clock controls acetaminophen bioactivation through NADPH-cytochrome P450 oxidoreductase. Proceedings of the National Academy of Sciences of the United States of America *111*, 18757-18762.
Kanehisa, M., and Goto, S. (2000). KEGG: kyoto encyclopedia of genes and genomes. Nucleic acids research *28*, 27-30.
Kim, Y.C., and Lee, S.J. (1998). Temporal variation in hepatotoxicity and metabolism of acetaminophen in mice. Toxicology *128*, 53-61.
Koike, N., Yoo, S.H., Huang, H.C., Kumar, V., Lee, C., Kim, T.K., and Takahashi, J.S. (2012). Transcriptional architecture and chromatin landscape of the core circadian clock in mammals. Science *338*, 349-354.
Langmead, B., Trapnell, C., Pop, M., and Salzberg, S.L. (2009). Ultrafast and memory-efficient alignment of short DNA sequences to the human genome. Genome Biol *10*, R25.
Leone, V., Gibbons, S.M., Martinez, K., Hutchison, A.L., Huang, E.Y., Cham, C.M., Pierre, J.F., Heneghan, A.F., Nadimpalli, A., Hubert, N.*, et al.* (2015). Effects of diurnal variation of gut microbes and high-fat feeding on host circadian clock function and metabolism. Cell host & microbe *17*, 681-689.
Levy, M., Thaiss, C.A., Zeevi, D., Dohnalova, L., Zilberman-Schapira, G., Mahdi, J.A., David, E., Savidor, A., Korem, T., Herzig, Y.*, et al.* (2015). Microbiota-Modulated Metabolites Shape the Intestinal Microenvironment by Regulating NLRP6 Inflammasome Signaling. Cell *163*, 1428-1443.
Li, J., Jia, H., Cai, X., Zhong, H., Feng, Q., Sunagawa, S., Arumugam, M., Kultima, J.R., Prifti, E., Nielsen, T.*, et al.* (2014). An integrated catalog of reference genes in the human gut microbiome. Nat Biotechnol *32*, 834-841.
Liang, X., Bushman, F.D., and FitzGerald, G.A. (2015). Rhythmicity of the intestinal microbiota is regulated by gender and the host circadian clock. Proceedings of the National Academy of Sciences of the United States of America *112*, 10479-10484.
Loonen, L.M., Stolte, E.H., Jaklofsky, M.T., Meijerink, M., Dekker, J., van Baarlen, P., and Wells, J.M. (2014). REG3gamma-deficient mice have altered mucus distribution and increased mucosal inflammatory responses to the microbiota and enteric pathogens in the ileum. Mucosal immunology *7*, 939-947.
Marco-Sola, S., Sammeth, M., Guigo, R., and Ribeca, P. (2012). The GEM mapper: fast, accurate and versatile alignment by filtration. Nature methods *9*, 1185-1188.
Masri, S., Papagiannakopoulos, T., Kinouchi, K., Liu, Y., Cervantes, M., Baldi, P., Jacks, T., and Sassone-Corsi, P. (2016). Lung Adenocarcinoma Distally Rewires Hepatic Circadian Homeostasis. Cell *165*, 896-909.
Minami, Y., Kasukawa, T., Kakazu, Y., Iigo, M., Sugimoto, M., Ikeda, S., Yasui, A., van der Horst, G.T., Soga, T., and Ueda, H.R. (2009). Measurement of internal body time by blood metabolomics. Proceedings of the National Academy of Sciences of the United States of America *106*, 9890-9895.
Mukherji, A., Kobiita, A., Ye, T., and Chambon, P. (2013). Homeostasis in intestinal epithelium is orchestrated by the circadian clock and microbiota cues transduced by TLRs. Cell *153*, 812-827.
Murakami, M., Tognini, P., Liu, Y., Eckel-Mahan, K.L., Baldi, P., and Sassone-Corsi, P. (2016). Gut microbiota directs PPARgamma-driven reprogramming of the liver circadian clock by nutritional challenge. EMBO Rep *17*, 1292-1303.
Nakahata, Y., Kaluzova, M., Grimaldi, B., Sahar, S., Hirayama, J., Chen, D., Guarente, L.P., and Sassone-Corsi, P. (2008). The NAD+-dependent deacetylase SIRT1 modulates CLOCK-mediated chromatin remodeling and circadian control. Cell *134*, 329-340.
Nakahata, Y., Sahar, S., Astarita, G., Kaluzova, M., and Sassone-Corsi, P. (2009). Circadian control of the NAD+ salvage pathway by CLOCK-SIRT1. Science *324*, 654-657.
Neufeld-Cohen, A., Robles, M.S., Aviram, R., Manella, G., Adamovich, Y., Ladeuix, B., Nir, D., Rousso-Noori, L., Kuperman, Y., Golik, M.*, et al.* (2016). Circadian control of oscillations in mitochondrial rate-limiting enzymes and nutrient utilization by PERIOD proteins. Proceedings of the National Academy of Sciences of the United States of America *113*, E1673-1682.

Panda, S., Antoch, M.P., Miller, B.H., Su, A.I., Schook, A.B., Straume, M., Schultz, P.G., Kay, S.A., Takahashi, J.S., and Hogenesch, J.B. (2002). Coordinated transcription of key pathways in the mouse by the circadian clock. Cell *109*, 307-320.
Panda, S., and Hogenesch, J.B. (2004). It's all in the timing: many clocks, many outputs. Journal of biological rhythms *19*, 374-387.
Perelis, M., Marcheva, B., Ramsey, K.M., Schipma, M.J., Hutchison, A.L., Taguchi, A., Peek, C.B., Hong, H., Huang, W., Omura, C*., et al.* (2015). Pancreatic beta cell enhancers regulate rhythmic transcription of genes controlling insulin secretion. Science *350*, aac4250.
Ramsey, K.M., Yoshino, J., Brace, C.S., Abrassart, D., Kobayashi, Y., Marcheva, B., Hong, H.K., Chong, J.L., Buhr, E.D., Lee, C*., et al.* (2009). Circadian clock feedback cycle through NAMPT-mediated NAD+ biosynthesis. Science *324*, 651-654.
Robertson, B.R., O'Rourke, J.L., Neilan, B.A., Vandamme, P., On, S.L., Fox, J.G., and Lee, A. (2005). Mucispirillum schaedleri gen. nov., sp. nov., a spiral-shaped bacterium colonizing the mucus layer of the gastrointestinal tract of laboratory rodents. International journal of systematic and evolutionary microbiology *55*, 1199-1204.
Thaiss, C.A., Levy, M., and Elinav, E. (2015a). Chronobiomics: The Biological Clock as a New Principle in Host-Microbial Interactions. PLoS pathogens *11*, e1005113.
Thaiss, C.A., Zeevi, D., Levy, M., Segal, E., and Elinav, E. (2015b). A day in the life of the meta-organism: diurnal rhythms of the intestinal microbiome and its host. Gut Microbes *6*, 137-142.
Thaiss, C.A., Zeevi, D., Levy, M., Zilberman-Schapira, G., Suez, J., Tengeler, A.C., Abramson, L., Katz, M.N., Korem, T., Zmora, N*., et al.* (2014). Transkingdom control of microbiota diurnal oscillations promotes metabolic homeostasis. Cell *159*, 514-529.
Trapnell, C., Pachter, L., and Salzberg, S.L. (2009). TopHat: discovering splice junctions with RNA-Seq. Bioinformatics *25*, 1105-1111.
Vaishnava, S., Yamamoto, M., Severson, K.M., Ruhn, K.A., Yu, X., Koren, O., Ley, R., Wakeland, E.K., and Hooper, L.V. (2011). The antibacterial lectin RegIIIgamma promotes the spatial segregation of microbiota and host in the intestine. Science *334*, 255-258.
Voigt, R.M., Forsyth, C.B., Green, S.J., Mutlu, E., Engen, P., Vitaterna, M.H., Turek, F.W., and Keshavarzian, A. (2014). Circadian disorganization alters intestinal microbiota. PloS one *9*, e97500.
Voigt, R.M., Summa, K.C., Forsyth, C.B., Green, S.J., Engen, P., Naqib, A., Vitaterna, M.H., Turek, F.W., and Keshavarzian, A. (2016). The Circadian Clock Mutation Promotes Intestinal Dysbiosis. Alcohol Clin Exp Res *40*, 335-347.
Vollmers, C., Schmitz, R.J., Nathanson, J., Yeo, G., Ecker, J.R., and Panda, S. (2012). Circadian oscillations of protein-coding and regulatory RNAs in a highly dynamic mammalian liver epigenome. Cell metabolism *16*, 833-845.
Wlodarska, M., Thaiss, C.A., Nowarski, R., Henao-Mejia, J., Zhang, J.P., Brown, E.M., Frankel, G., Levy, M., Katz, M.N., Philbrick, W.M*., et al.* (2014). NLRP6 inflammasome orchestrates the colonic host-microbial interface by regulating goblet cell mucus secretion. Cell *156*, 1045-1059.
Zarrinpar, A., Chaix, A., Yooseph, S., and Panda, S. (2014). Diet and feeding pattern affect the diurnal dynamics of the gut microbiome. Cell metabolism *20*, 1006-1017.
Zhang, R., Lahens, N.F., Ballance, H.I., Hughes, M.E., and Hogenesch, J.B. (2014). A circadian gene expression atlas in mammals: implications for biology and medicine. Proceedings of the National Academy of Sciences of the United States of America *111*, 16219-16224.
Zwighaft, Z., Aviram, R., Shalev, M., Rousso-Noori, L., Kraut-Cohen, J., Golik, M., Brandis, A., Reinke, H., Aharoni, A., Kahana, C*., et al.* (2015). Circadian Clock Control by Polyamine Levels through a Mechanism that Declines with Age. Cell metabolism *22*, 874-885.

STAR Methods

Key Resources Table

REAGENT or RESOURCE	SOURCE	IDENTIFIER
Antibodies		
anti-H3K4me2	Abcam	Cat#ab32356
anti-H3K4me3	Millipore	Cat#07-473
anti-H3K27ac	Abcam	Cat#ab4729
Chemicals, Peptides, and Recombinant Proteins		
Vacomycin	Sigma-Aldrich	Cat#V1130
Ampicillin	Sigma-Aldrich	Cat#A1593
Kanamycin	Sigma-Aldrich	Cat#60615
Metronidazole	Sigma-Aldrich	Cat#M3761
Acetaminophen	Sigma-Aldrich	Cat#A7085
Deposited Data		
Raw data files for 16S sequencing	European nucleotide archive (ENA)	PRJEB16726
Raw data files for metagenomic sequencing	European nucleotide archive (ENA)	PRJEB16726
Raw data files for RNA sequencing	European nucleotide archive (ENA)	PRJEB16726
Experimental Models: Organisms/Strains		
C57Bl/6JOlaHsd	Harlan	Cat#705
B6.129-Reg3g$^{tm1.1Lvh}$/J	Jackson Laboratories	Cat#017480
Per1/2	Gad Asher (Weizmann Institute)	(Adamovich et al., 2014)
Sequence-Based Reagents		
111-967F-PP: CNACGCGAAGAACCTTANC	IDT	16S qPCR
112-967F-UC3: ATACGCGARGAACCTTACC	IDT	16S qPCR
113-967F-AQ: CTAACCGANGAACCTYACC	IDT	16S qPCR
114-967F-S: CAACGCGMARAACCTTACC	IDT	16S qPCR
115-1046R-S: CGACRRCCATGCANCACCT	IDT	16S qPCR
GCTGCCTCCCGTAGGAGT, dual labeled, 5' CAL flour Red 610, 3' BHQ-2	Stellaris	16S FISH
CGATTGAGGCCGGTAATACGACTCACTATAGGGGCGACGT GTGCTCTTCCGATCTXXXXXXXXT modified with a C3 spacer (blocker) at the 5'	(Gury-BenAri et al., 2016)	Chromatin first indexing adapter
XXXXNNNNNAGATCGGAAGAGCGTCGTGTAG modified with a phosphate group at 5' and a C3 spacer (blocker) at the 3'	(Gury-BenAri et al., 2016)	Ligation adapter
TCTAGCCTTCTCGCAGCACATC	(Gury-BenAri et al., 2016)	Second primer

AATGATACGGCGACCACCGAGATCTACACTCTTTCCCTACAC	(Gury-BenAri et al., 2016)	P5_Rd1
CAAGCAGAAGACGGCATACGAGATGTGACTGGAGTTCAGAC	(Gury-BenAri et al., 2016)	P7_Rd2
Software and Algorithms		
NIH's Database for Annotation, Visualization and Integrated Discovery	(Dennis et al., 2003)	https://david.ncifcrf.gov/
QIIME	(Caporaso et al., 2010)	http://qiime.org
Trimmomatic	(Bolger et al., 2014)	http://www.usadellab.org/cms/?page=trimmomatic
TopHat (v2.0.10)	(Trapnell et al., 2009)	https://ccb.jhu.edu/software/tophat/index.shtml
HOMER software	(Heinz et al., 2010)	http://homer.salk.edu

Methods and Resources

Contact for reagent and resource sharing

Further information and requests for reagents may be directed to, and will be fulfilled by the corresponding authors Eran Segal (eran.segal@weizmann.ac.il) and Eran Elinav (eran.elinav@weizmann.ac.il).

Experimental model and subject details

Mice

C57Bl/6 mice were purchased from Harlan and allowed to acclimatize to the animal facility environment for 2 weeks before used for experimentation. Germ-free C57Bl/6 mice were born in the Weizmann Institute germ-free facility and routinely monitored for sterility. Mice lacking RegIIIγ (B6.129-Reg3g$^{tm1.1Lvh}$/J) were obtained from The Jackson Laboratory. *Per1/2*-deficient mice on a C57Bl/6 background were kindly provided by Gad Asher (Weizmann Institute). In all experiments, age- and gender-matched mice were used. Mice were 8-9 weeks of age at the beginning of experiments. All mice were kept at a strict 24-hour light-dark cycle, with lights being turn on from 6am to 6pm. In timed feeding experiments, food access was limited to the dark phase or light phase where indicated. Polyamine-deficient diet was applied for one month. For antibiotic treatment, mice were given a combination of vancomycin (0.5 g/l), ampicillin (1 g/l), kanamycin (1 g/l), and metronidazole (1 g/l) in

their drinking water for three weeks as previously described (Levy et al., 2015). Acetaminophen was administered intraperitoneally at a concentration of 500 mg/kg at either ZT0 or ZT12, and mice were analyzed 10 hours after injection. All antibiotics as well as acetaminophen were obtained from Sigma Aldrich.

Food intake and other metabolic parameters were measured using the PhenoMaster system (TSE-Systems, Bad Homburg, Germany), which consists of a combination of sensitive feeding sensors for automated measurement and a photobeam-based activity monitoring system detects oxygen and carbon dioxide consumption, and records ambulatory movements, including rearing and climbing, in each cage. All parameters were measured continuously and simultaneously. Mice were trained singly-housed in identical cages prior to data acquisition.

All experimental procedures were approved by the local IACUC.

Method details

Scanning electron microscopy

Mice were perfused with fixative containing 2% glutaraldehyde and 3% PFA in 0.1M sodium cacodylate. Colonic samples were extensively washed from fecal matter and fixed for 24hrs. Samples were rinsed three times in sodium cacodylate buffer and postfixed in 1% osmiumtetroxide for 1hr, stained in 1% uranyl acetate for a further hour, then rinsed, dehydrated, and dried using critical point drying. Samples were then gold-coated and viewed in an ULTRA 55 FEG (ZEISS). For image quantification, the bacteria on randomly selected fields per sample were counted and averaged.

16S qPCR protocol for quantification of bacterial DNA

Colons were extensively cleaned from fecal material, and DNA was extracted using MoBio PowerSoil kit. DNA concentration was calculated using a standard curve of known DNA concentrations from E.coli K12. 16S qPCR using primers identifying different regions of the V6 16S gene was performed using Kappa SYBR fast mix, using the following primer sequences:

111-967F-PP: CNACGCGAAGAACCTTANC
112-967F-UC3: ATACGCGARGAACCTTACC
113-967F-AQ: CTAACCGANGAACCTYACC
114-967F-S: CAACGCGMARAACCTTACC

115-1046R-S: CGACRRCCATGCANCACCT

Absolute numbers of bacteria in the samples were then approximated as DNA amount in a sample/DNA molecule mass of bacteria.

Immunofluorescence

For fluorescent visualization of bacteria, colon samples were fixed using freshly prepared Carnoy's fixative (60% EtOH, 30% Chloroform, 10% glacial acetic acid) for 2 hours, at 4°C, followed by a wash with 100% EtOH and storage in 100% EtOH until paraffin embedding and section. Colon sections were hybridized with 16S probe at a concentration of 10ng/µl over night at 50°C, diluted in hybridization buffer (20mM Tris-HCl (PH 7.4), 0.9M NaCl, 0.1%SDS.

Probe sequence: GCTGCCTCCCGTAGGAGT, dual labeled, 5' CAL flour Red 610, 3' BHQ-2.

For co-immunostaining, tissue sections were blocked at room temperature for 30 min in $PBS^{-/-}$, 0.05% Triton and 20% normal horse serum, followed by incubation with anti-Muc2 antibody (H300 Santa Cruz), 1:200 in $PBS^{-/-}$, 0.05% Triton and 2% normal horse serum, over night at 4°C. Sections were then washed in PBS and incubated with a secondary Ab, 1:400, 2 hrs at room temperature. Samples were then washed and mounted. Visualization was performed using a Nikon Eclipse Ti microscope.

Taxonomic microbiota analysis

Frozen fecal samples were processed for DNA isolation using the MoBio PowerSoil kit according to the manufacturer's instructions. For the 16S rRNA gene PCR amplification, 1ng of the purified fecal DNA was used for PCR amplification. Amplicons spanning the variable region 1/2 (V1/2) of the 16S rRNA gene were generated by using the following barcoded primers: Fwd 5'-XXXXXXXXAGAGTTTGATCCTGGCTCAG-3', Rev 5'-TGCTGCCTCCCGTAGGAGT-3', where X represents a barcode base. The reactions were subsequently pooled and cleaned (PCR clean kit, Promega), and the PCR products were then sequenced on an Illumina MiSeq in 500 bp paired-end method. The reads were then processed using the QIIME (Quantitative Insights Into Microbial Ecology, http://www.qiime.org) analysis pipeline as described (Levy et al., 2015). In brief, fasta quality files and a mapping file indicating the barcode sequence corresponding to each sample were used as inputs, reads were split by samples according to the barcode, taxonomical classification was performed using the RDP-classifier, and an OTU table was created. Closed-reference OTU mapping was employed using the Greengenes database. Rarefaction was used to exclude samples with insufficient count of reads

per sample. Sequences sharing 97% nucleotide sequence identity in the V2 region were binned into operational taxonomic units (97% ID OTUs). For beta-diversity, weighted unifrac measurements were plotted according to the first two principal coordinates based on 10,000 reads per sample.

Metagenomic analysis

We filtered metagenomic reads containing Illumina adapters, filtered low quality reads and trimmed low quality read edges. We detected host DNA by mapping with GEM (Marco-Sola et al., 2012) to the mouse genome with inclusive parameters, and removed those reads. We assigned length-normalized RA of genes, obtained by similar mapping with GEM to a reference catalog (Li et al., 2014), to KEGG Orthology (KO) entries (Kanehisa and Goto, 2000), and these were then normalized to a sum of 1. We calculated RA of KEGG modules and pathways by summation. We considered only samples with >100K metagenomics reads.

Quality control of metagenomic reads and removal of host DNA

We applied Trimmomatic (Bolger et al., 2014) with the following parameters:

ILLUMINACLIP:<Trueseq3 adapters fasta file>:2:30:10 LEADING:25 TRAILING:25 MINLEN:50. We removed host DNA by mapping to the mouse genome (mm10, downloaded from https://genome.ucsc.edu) and removing any mapped reads (see section below).

Functional assignment of metagenomic reads

Reads mapped to the gut microbial gene catalog were assigned a KEGG (Kanehisa and Goto, 2000). Genes were subsequently mapped to KEGG modules and pathways. For the KEGG pathway analysis, only pathways whose gene coverage was above 0.2 were included. Bacterial assignment to metabolic pathways was done by mapping of metagenomic reads to genes from the respective metagenomic modules. Mapped reads were extracted and re-mapped to a bacterial genomes database. Reads that were successfully mapped were grouped into genera, and those not mapped were marked as 'unknowns'.

RNA-seq processing and analysis

We used a derivation of MARS-seq as described (Jaitin et al., 2014), developed for single-cell RNA-seq to produce expression libraries with a minimum of two replicates per group. We aligned the RNA-seq reads to the mouse reference genome (NCBI 37, mm9) using TopHat v2.0.13 with default parameters (Trapnell et al., 2009). Duplicate reads were filtered if they aligned to the same base and had identical UMIs. Expression levels were calculated and normalized for each sample to the total number of reads using HOMER software (http://homer.salk.edu) with the command "analyzeRepeats.pl rna mm9 -d [sample files] -count 3utr -condenseGenes" (Heinz et al., 2010). KEGG analysis was done using DAVID (Dennis et al., 2003). For the generation of heatmaps, genes were normalized to their mean expression across all time points.

iChIP-IVT

We used a recently developed protocol for ChIP-seq involving amplification by in-vitro transcription (Gury-BenAri et al., 2016). Sorted epithelial cells were cross-linked for 8 min in 1% formaldehyde and quenched for 5 min in 0.125 M glycine prior to sorting. Sorted and frozen cell pellets were lysed in 0.5% SDS and sheared with the NGS Bioruptor Sonicator (Diagenode). Sheared chromatin was immobilized on 12 µl Dynabeads Protein G (Invitrogen) with 1.3 µg of anti-H3 antibody (ab1791). Magnetized chromatin was then washed with 10 mM Tris-HCl supplemented with 1X protease inhibitors. Chromatin was end repaired, dA-tailed and ligated with 5 µl of 0.75 µM partial Illumina Read2 sequencing adapters containing T7 polymerase promotor. Indexed chromatin was pooled, split to 3 IP pools and incubated with 2.5 µg anti-H3K4me2 antibody (ab32356)/anti-H3K4me3 (Millipore, 07-473)/anti-H3K27Ac (ab4729) at 4°C for 3h and for an additional hour with Protein G magnetic beads (Invitrogen). Magnetized chromatin was washed and reverse cross-linked. DNA was subsequently purified with 1.65X SPRI. In vitro transcription step of linear amplification were introduced to produce RNA transcripts out of the DNA fragments using the T7 High Yield RNA polymerase IVT kit (NEB). After IVT, DNAse treatment was performed to eliminate the DNA fragments. Next, a partial Illumina Read1 sequencing adapter that includes a pool barcode was single strand ligated to the fragmented RNA using a T4 RNA ligase I (New England Biolabs). The ligated product was reverse transcribed using Affinity Script RT enzyme (Agilent) and a primer complementary to the ligated adapter. The library was completed and amplified through a PCR reaction with 0.5 µ M of each primer and PCR ready mix (Kapa Biosystems). The forward primer contains the Illumina P5-Read1 sequences and the reverse primer contains the P7-Read2 sequences. DNA concentration was measured with a Qubit fluorimeter (Invitrogen) and mean molecule size was determined with 2200 TapeStation analyzer (Agilent) and library quality was further determined by qPCR.

The following primer sequences were used:

Primer name	Sequence and modifications
Chromatin first indexing adapter	CGATTGAGGCCGGTAATACGACTCACTATAGGGGCGACGTGTGCTCTTCCGATCT XXXXXXXXT modified with a C3 spacer (blocker) at the 5'. XXXXXXXX is the barcode for sample multiplexing.
Ligation adapter	XXXXNNNNNNAGATCGGAAGAGCGTCGTGTAG modified with a phosphate group at 5' and a C3 spacer (blocker) at the 3'.
Second primer	TCTAGCCTTCTCGCAGCACATC
P5_Rd1	AATGATACGGCGACCACCGAGATCTACACTCTTTCCCTACAC
P7_Rd2	CAAGCAGAAGACGGCATACGAGATGTGACTGGAGTTCAGAC

Processing of ChIP-seq

Reads were aligned to the mouse reference genome (mm9, NCBI 37) using Bowtie2 aligner version 2.2.5 (Langmead et al., 2009) with default parameters. The Picard tool MarkDuplicates from the Broad Institute (http://broadinstitute.github.io/picard/) was used to remove PCR duplicates. To identify regions of enrichment (peaks) from ChIP-seq (H3K4me2, H3K4me3, H3K27ac), we used the HOMER package makeTagDirectory followed by findPeaks command with the histone parameter or 500bp centered regions, respectively (Heinz et al., 2010). Union peaks file were generated for each of H3K4me2 and H3K4me3 by combining and merging overlapping peaks in all samples.

Chromatin analysis

The read density (number of reads in 10 million total reads per 1000 bp) was calculated in each region from the union peaks files. The region intensity was calculated by quantile normalization (across samples) of the read density in log base 2 (log2(x+1)). We considered promoters to be H3K4me3 regions within +/- 2000bp of a TSS and candidate enhancers to be distal H3K4me2 regions. Enhancers were assigned to the nearest gene within 50kb. The activity level of promoters and enhancers was determined by the H3K27ac intensity within the H3K4me3 or H3K4me2 region, respectively.

Gene tracks and normalization

All gene tracks were visualized as bigWig files of the combined replicates normalized to 10,000,000 reads and created by the HOMER algorithm makeUCSCfile (Heinz et al., 2010). For visualization, the tracks were smoothed by averaging over a sliding window of 500 bases.

Metabolomics

Cecal samples were collected, immediately frozen in liquid nitrogen and stored at -80^{o}C. Samples were prepared using the automated MicroLab STAR® system from (Hamilton). To remove protein, dissociate small molecules bound to protein or trapped in the precipitated protein matrix, and to recover chemically diverse metabolites, proteins were precipitated with methanol. The resulting extract was divided into five fractions: one for analysis by UPLC-MS/MS with positive ion mode electrospray ionization, one for analysis by UPLC-MS/MS with negative ion mode electrospray ionization, one for LC polar platform, one for analysis by GC-MS, and one sample was reserved for backup. Samples were placed briefly on a TurboVap® (Zymark) to remove the organic solvent. For LC, the samples were stored overnight under nitrogen before preparation for analysis. For GC, each sample was dried under vacuum overnight before preparation for analysis.

Data Extraction and Compound Identification: Raw data was extracted, peak-identified and QC processed using Metabolon's hardware and software. Compounds were identified by comparison to library entries of purified standards or recurrent unknown entities. Metabolite Quantification and Data Normalization: Peaks were quantified using area-under-the-curve. For studies spanning multiple days, a data normalization step was performed to correct variation resulting from instrument inter-day tuning differences.

For targeted analysis of polyamines and amino acids, 50 µl of serum were diluted 100 µl 0.1% formic acid in acetonitrile. After cooling on ice for 10 minutes, the samples were centrifuged, and 10 µl of the supernatant was added to 70 µl of borate buffer and derivatized using the AccQTag method (Boughton et al., 2011). The LC-MS/MS instrument consisted of Acquity I-class UPLC system and Xevo TQ-S triple quadrupole mass spectrometer (Waters). Chromatographic separation and mass detection were carried out in the conditions recently described (Zwighaft et al., 2015) with adjustments to obtain the highest signal for each compound.

Histology

Sections from the left lobe of the liver were fixed in paraformaldehyde and embedded in paraffin for staining with H&E. Subsequently, sections were examined by a blinded veterinary pathologist and scored for necrosis and hemorrhage on a scale from 0 (healthy) to 3 (most severe).

Statistical analysis

Data are expressed as mean ± SEM. Cycling behavior was assessed using JTK_cycle (Hughes et al., 2010), with oscillations tested for a 24 hour period length. Unless stated otherwise, elements with $p<0.05$ and $q<0.1$ were considered significant. For metabolites, $q<0.2$ was considered significant. For two-group comparisons, Mann-Whitney *U*-test was used and comparisons with $p<0.05$ were considered significant. Analysis of shared and unique oscillatory transcripts was performed on balanced groups to account for the sensitivity of JTK_cycle to the number of replicates. This was done by random sub-sampling of samples at each time point, performed 250 times. Hence, average numbers are presented. Significance and numbers of the fraction of shared oscillating transcripts out of total oscillating transcripts in colon and liver tissues was determined by permutations followed by re-running of the JTK_cycle algorithm. In each permutation samples were randomly selected at each time point from both antibiotic-treated and controlled mice, maintaining balance both in the number of replicates and in the number of replicates belonging to each group across time points.

Figure legends

Figure 1. Mucosal proximity of the intestinal microbiota undergoes diurnal fluctuations

(A) Schematic showing sampling times for luminal and mucosal-adherent communities.

(B) SEM images showing diurnal fluctuations in epithelial colonization by bacteria. Images are representative of 10 randomly chosen views per mouse.

(C) Diurnal fluctuations in the number of bacteria attached to colonic epithelium over two dark-light cycles as determined by bacterial qPCR of adherent communities.

(D) Relative taxonomic composition of mucosal-adherent bacteria over the course of two light-dark cycles.

(E) Principal coordinate analysis (PCoA) of mucosal-adherent bacteria over the course of two light-dark cycles.

(F) Epithelial-adherent operational taxonomic units (OTUs) showing diurnal oscillations in absolute abundance. Fluctuation amplitudes are depicted. Dashed line indicates $q<0.1$.

(G) Example of a bacterial species showing fluctuating absolute numbers in mucosal-adherent communities.

(H, I) Dot plot (H) and heatmap (I) of diurnal gene abundance oscillations in mucosal commensal bacteria. Genes with $p<0.05$ and $q<0.1$ are shown.

Data are representative of two independent experiments with N=45 (A-G) or N=18 mice (H, I) mice. JTK_cycle was used to calculate p- and q-values.

See also **Figure S1**.

Figure 2. Bacterial motility and mucus degradation undergoes diurnal fluctuations

(A) KEGG pathways of mucosal-associated microbial communities showing diurnal oscillations in relative abundance.

(B) Diurnal fluctuations in the relative abundance of bacterial chemotaxis in mucosal-associated communities.

(C, D) Quantification (C) and representative immunofluorescence images (D) showing diurnal fluctuations in epithelial proximity by commensal bacteria. Stained are Muc2 protein (green) and bacterial 16S rDNA (red). Images are representative of 10 randomly chosen views per mouse. Arrows indicate bacterial invasion into the mucus layer. Scale bars indicate 100 µm.

(E) Comparative immunofluorescence images showing epithelial proximity of commensal bacteria in wild-type and *Reg3g*$^{-/-}$ mice at ZT12.

(F) Fluctuations in the number of bacteria attached to intestinal epithelium in wild-type and *Reg3g*$^{-/-}$ mice over two dark-light cycles as determined by bacterial qPCR of adherent communities.

(G, H) Numbers of mucosal-resident bacteria in *Per1/2*$^{-/-}$ mice that were either fed ad libitum (G) or only during the light phase (H).

(I) Epithelial-adherent operational taxonomic units (OTUs) showing diurnal oscillations in relative abundance in *Per1/2*$^{-/-}$ mice that were either fed ad libitum or only during the light phase.

Data are representative of 1-2 independent experiments with N=18-45 mice. JTK_cycle was used to calculate p- and q-values.

See also **Figure S2** and **Tables S1 and S2**.

Figure 3. Antibiotic treatment abrogates microbial adherence rhythms and reprograms intestinal transcriptome oscillations

(A) Schematic showing sampling times for colonic transcriptome, epigenome, and metabolome in antibiotics-treated mice and controls.

(B) Diurnal fluctuations in the number of bacteria attached to colonic epithelium over the course of two dark-light cycles in antibiotics-treated mice and controls.

(C) Representative SEM images showing epithelial colonization by bacteria at ZT0 in antibiotics-treated mice and controls.

(D) Epithelial-adherent OTUs showing diurnal oscillations in relative abundance in antibiotics-treated mice and controls.

(E) Relative taxonomic composition of mucosal-adherent bacteria in antibiotics-treated mice over the course of two light-dark cycles. See Figure 1D for comparison to control mice.

(F) Venn diagram of shared and unique oscillating colonic transcripts of antibiotics-treated mice compared to controls, $p<0.05$ and $q<0.1$. The sets of oscillating transcripts are significantly non-overlapping ($p<0.03$).

(G-I) Heatmap representation of shared cycling colonic transcripts between antibiotics-treated mice and controls (G), of transcripts uniquely cycling in control mice (H), and of transcripts uniquely oscillating in antibiotics-treated mice (I), $p<0.05$ and $q<0.1$.

(J-L) KEGG analysis of shared cycling colonic transcripts between antibiotics-treated mice and controls (J), of transcripts uniquely cycling in control mice (K), and of transcripts uniquely oscillating in antibiotics-treated mice (L).

Data are representative of two independent experiments with N=27-45 mice. JTK_cycle was used to calculate p- and q-values.

See also **Figure S3**.

Figure 4. Antibiotic treatment reprograms chromatin oscillations in intestinal epithelial cells

(A) Schematic showing sampling times for epithelial ChIP-seq analysis. Assayed histone marks for enhancers, promoters, and active regions are indicated.

(B) H3K27ac peaks in H3K4me3 regions showing diurnal oscillations in antibiotics-treated and control mice, compared to stochastic oscillations in whole-cell extracts (WCE).

(C) Venn diagram of shared and unique active promoters oscillations in intestinal epithelial cells of antibiotics-treated mice and controls, $p<0.05$.

(D) Diurnal oscillations in normalized H3K4m3 peaks found in the 100 kb region of the *Dbp* locus in control (left) and antibiotics-treated mice (right).

(E, F) Heatmaps of active promoter oscillations that are lost (E) and gained (F) upon microbiota depletion.

(G) H3K27ac peaks at enhancers undergoing diurnal oscillations in intestinal epithelial cells of antibiotics-treated and control mice.

(H) Venn diagram of shared and unique active enhancer oscillations in intestinal epithelial cells of antibiotics-treated and control mice.

(I-L) Examples of gained (I, J) or lost (K, L) enhancer activity that correlates with gene expression rhythmicity.

Data are from N=18-45 mice. JTK_cycle was used to calculate p- and q-values.

See also **Figure S4**.

Figure 5. Reprogramming of the colonic and hepatic circadian transcriptome

(A) Schematic luminal and adherent variants of the same bacterial species.

(B) Quantification of mucosal-resident mouse and rat SFB after mono-inoculation of germ-free mice. Data are pooled from several time points. **** denotes $p<0.0001$ by Mann-Whitney *U*-test

(C) Numbers of mucosal-resident bacteria over 48 hours in germ-free mice that were mono-colonized with either mouse SFB or rat SFB.

(D) Overlap of cycling genes in the colons of *Reg3g*$^{-/-}$ mice, mouse SFB-colonized mice, and rat SFB-colonized mice with genes uniquely oscillating in either antibiotics-treated mice or controls.

(E) Rhythmic colonic gene expression of *Dbp* in the indicated groups.

(F) KEGG analysis of shared cycling colonic transcripts between mouse SFB mono-colonized mice and conventional controls.

(G) Schematic showing sampling times for intestinal and serum metabolite as well as liver transcriptome analysis.

(H) Venn diagram of shared and unique oscillating hepatic transcripts of antibiotics-treated mice compared to controls, $p<0.05$ and $q<0.1$. The sets of oscillating transcripts are significantly non-overlapping ($p<0.005$).

(I) KEGG analysis of shared cycling hepatic transcripts between antibiotics-treated mice and controls.

(J) Rhythmic hepatic gene expression of *Nr1d1* in antibiotics-treated mice and controls.

(K, L) KEGG analysis of hepatic transcripts uniquely cycling in control mice (K) and in antibiotics-treated mice (L). Inset in K shows gene expression of *Gpi1*.

Data are representative of 1-2 independent experiments with N=18-36 mice. JTK_cycle was used to calculate p- and q-values.

See also **Figure S5**.

Figure 6. Diurnal patterns of the microbiota metabolome influence systemic metabolite oscillations

(A) Heatmap of metabolites undergoing significant oscillations, $p<0.05$ and $q<0.2$. Examples for each cluster are indicated.

(B) Depiction of rhythmic elements in the bacterial pathway converting ornithine to proline.

(C) Depiction of rhythmic elements along the bacterial biotin biosynthetic pathway.

(D) Correlation of p-values for rhythmicity of amino acids and polyamines in the intestinal lumen and serum.

(E) Example of metabolites oscillating in intestinal lumen and serum with different phases.

(F) Quantification of significantly oscillating amino acids and polyamines in the sera of controls, antibiotics-treated mice, germ-free mice, ad libitum-fed *Per1/2*$^{-/-}$ mice, and light phase-fed *Per1/2*$^{-/-}$ mice.

(G-I) Diurnal oscillations of ornithine abundances in the sera of controls (G), antibiotics-treated and germ-free mice (H), and ad libitum-fed or light phase-fed *Per1/2*$^{-/-}$ mice (I).

Data are representative 1-2 experiments with N=18 mice. JTK_cycle was used to calculate p- and q-values.

See also **Figure S6**.

Figure 7. The microbiota impacts diurnal liver function and hepatotoxicity

(A) Schematic showing sampling times for serum metabolites and liver transcriptomes of mice fed a polyamine-deficient (PD) diet.

(B) Heatmap of oscillating serum amino acids and polyamines in mice fed a PD diet and controls.

(C) Venn diagram of shared and unique oscillating hepatic transcripts of mice fed a PD diet compared to controls, $p<0.05$ and $q<0.1$.

(D) Overlap of cycling genes in the livers of mice on a PD diet with genes uniquely oscillating in either antibiotics-treated mice or controls.

(E-G) Heatmap representation of shared cycling colonic transcripts between mice fed a PD diet and controls (G), of transcripts uniquely cycling in control mice (H), and of transcripts uniquely oscillating in PD diet mice (I), $p<0.05$ and $q<0.1$.

(H-K) Serum levels of liver enzymes (H, I), liver histology score (J), and representative histological images (K) of control, antibiotics-treated (Abx), and germ-free mice (GF) that were injected with APAP at ZT0 or ZT12. ** denotes $p<0.01$ and **** denotes $p<0.0001$ by Mann-Whitney *U*-test. Scale bars indicate 100 µm.

Data in A-G were obtained with N=18-36 mice. Data in H-K are representative of 3 independent experiments with N=4-10 mice in each groups. JTK_cycle was used to calculate p- and q-values.

See also **Figure S7**.

Supplemental figure legends

Figure S1. Diurnal fluctuations in the number and composition of mucosal-associated commensals, related to Figure 1

(A, B) SEM images (A) and quantification (B) showing diurnal fluctuations in epithelial colonization by bacteria. Images are representative of 10 randomly chosen views per mouse.
(C) Diurnal fluctuations in the number of bacteria attached to colonic epithelium determined every 4 hours over one light-dark cycle.
(D) Unweighted UniFrac distances of the initial time point compared to all other time points over the course of two light-dark cycles.
(E, F) Diurnal rhythmicity of beta-diversity of mucosal-adherent bacteria, as shown by PCoA of samples obtained from two consecutive dark-light phases. ZT12' indicates ZT12 on the following day.
(G) Absolute numbers of taxonomic composition of mucosal-adherent bacteria over the course of two light-dark cycles.
(H, I) Examples of bacterial species showing fluctuating absolute numbers in mucosal-adherent communities.
Data are representative of two independent experiments with N=45 mice. Panel C is from one experiment with N=35 mice. JTK_cycle was used to calculate p-values.

Figure S2. Diurnal fluctuations in bacterial motility and mucus degradation, related to Figure 2

(A) KEGG modules of the mucosal microbial community showing diurnal oscillations in relative abundance. Selected modules and genes are highlighted in red.
(B) Diurnal fluctuations in the relative abundance of flagellar assembly in mucosal-associated communities.
(C) Diurnal fluctuations in the relative abundance of Deferribacteriaceae in mucosal-associated communities.
(D) Immunofluorescence images showing diurnal fluctuations in epithelial proximity by commensal bacteria. Stained are Muc2 protein (green) and bacterial 16S rDNA (red). Images are representative of 10 randomly chosen views per mouse. Scale bars indicate 100 μm.
(E) Quantification of diurnal fluctuations in epithelial proximity by commensal bacteria in *Reg3g*$^{-/-}$ mice. Wild-type controls are shown in grey for comparison.
(F) Unweighted UniFrac distances of the initial time point compared to all other time points in *Reg3g*$^{-/-}$ mice over the course of two light-dark cycles. See Figure S1D for comparison to wild-type mice.

(G, H) Heatmap (G) and representative example (H) of oscillating OTUs in *Per1/2*$^{-/-}$ mice that were either fed ad libitum or only during the light phase.

(I) Diurnal fluctuations in the number of bacteria attached to colonic epithelium in wild-type mice fed either during the dark phase or during the light phase.

Data are representative of 1-2 independent experiments with N=18-45 mice. JTK_cycle was used to calculate p- and q-values.

Figure S3. The microbiota is required for coordinated oscillations in the intestinal transcriptome, related to Figure 3

(A) Representative SEM images of epithelial colonization by bacteria over the course of a day in antibiotics-treated mice. See Figure 1B for comparison to control mice.

(B) PCoA of mucosal-adherent communities in antibiotics-treated mice every 6 hours over the course of one day. See Figures S1E and S1F for comparison to control mice.

(C) UniFrac distance of the initial time point compared to all other time points over the course of two light-dark cycles in antibiotics-treated mice. See Figure S1D for comparison to control mice.

(D) Colonic expression of *Il18, Reg3b,* and *Reg3g* in antibiotics-treated mice and controls. Data are pooled from several time points. **** denotes p<0.0001 by Mann-Whitney *U*-test

(E) Venn diagram of shared and unique oscillating colonic transcripts of antibiotics-treated mice compared to controls sampled every 4 hours over 24 hours.

(F, G) 48-hour recordings of rhythmic oxygen consumption (F) and food intake (G) in antibiotics-treated mice and controls.

(H) Average colonic expression levels in antibiotics-treated mice and controls of genes that are cycling in either both conditions (shared), only in controls, or only in antibiotics (Abx)-treated mice.

(I) Rhythmicity analysis in the mucosal microbiota of KEGG pathways that acquire rhythmicity in colonic transcripts upon antibiotic treatment.

Data are representative of 1-2 independent experiments with N=45 mice.

Figure S4. The impact of the microbiota on the diurnal epigenetic landscape, related to Figure 4

(A) Heatmap representation of cycling active promoter marks compared to genomic background in whole-cell extracts.

(B) Diurnal oscillations in normalized H3K4me3 peaks (left) and H3K27ac peaks (right) found in the 100 kb region of the *Nr1d1* locus.

(C) Rhythmic colonic gene expression of *Dbp* in control and antibiotics-treated mice.

(D) Examples of shared (left), lost (middle), and gained (right) oscillations in active promoters (above) and gene expression (below) in antibiotics-treated mice compared to controls.
(E) H3K4me2 peaks at enhancers undergoing diurnal oscillations in intestinal epithelial cells of antibiotics-treated and control mice. Dashed line indicates $p<0.05$.
(F) Venn diagram of shared and unique enhancer usage oscillations in intestinal epithelial cells of antibiotics-treated and control mice.
(G, H) Example of gene with H3K4me2 peak oscillation in the control group (G), but H3K27ac oscillation at enhancer (G) and rhythmic gene expression (H) uniquely in antibiotics-treated mice.
Data are from N=18-45 mice. JTK_cycle was used to calculate p- and q-values.

Figure S5. The impact of the microbiota on hepatic transcriptome oscillations, related to Figure 5

(A-C) Heatmap representation of shared cycling hepatic transcripts between antibiotics-treated mice and controls (A), of transcripts uniquely cycling in control mice (B), and of transcripts uniquely oscillating in antibiotics-treated mice (C), $p<0.05$ and $q<0.1$.
(D) Hepatic expression levels in antibiotics-treated mice and controls of genes that are cycling in either both conditions (shared), only in controls, or only in antibiotics-treated mice.
(E) Rhythmic hepatic gene expression of *Per2* in antibiotics-treated mice and controls.
(F) Overlap of cycling genes in the livers of germ-free mice with genes uniquely oscillating in either antibiotics-treated mice or controls.
Data are representative of 1-2 independent experiments with N=18-36 mice. JTK_cycle was used to calculate p- and q-values.

Figure S6. Intestinal and systemic metabolite oscillations, related to Figure 6

(A-C) Examples of metabolites oscillating in the intestinal lumen.
(D) Depiction of rhythmic elements along the bacterial sucrose degradation pathway.
(E-G) Examples of amino acids oscillating in intestinal lumen and serum.
(H-J) Heatmap (H) and examples (I, J) of amino acids and polyamines in the serum of ad libitum-fed or light phase-fed *Per1/2*$^{-/-}$ mice.
Data are from 1-2 experiments with N=18 mice. JTK_cycle was used to calculate p- and q-values.

Figure S7. The impact of the microbiota and metabolites on circadian liver function, related to Figure 7

(A-C) Examples of serum amino acids and polyamines losing oscillations upon feeding with a polyamine-deficient (PD) diet.

(D-G) Serum levels of liver enzymes (D, E) liver histology score (F), and representative histological images (G) from *Per1/2*$^{-/-}$ mice and wild-type controls that were injected with APAP at ZT0 or ZT12.

Data are representative of 1-2 independent experiments with N=18-36 mice.

Supplemental table legends

Table S1. Bacterial species contributing to diurnal oscillations in bacterial chemotaxis (KO02030), related to Figure 2

Table S2. Bacterial species contributing to diurnal oscillations in flagellar assembly (KO02040), related to Figure 2

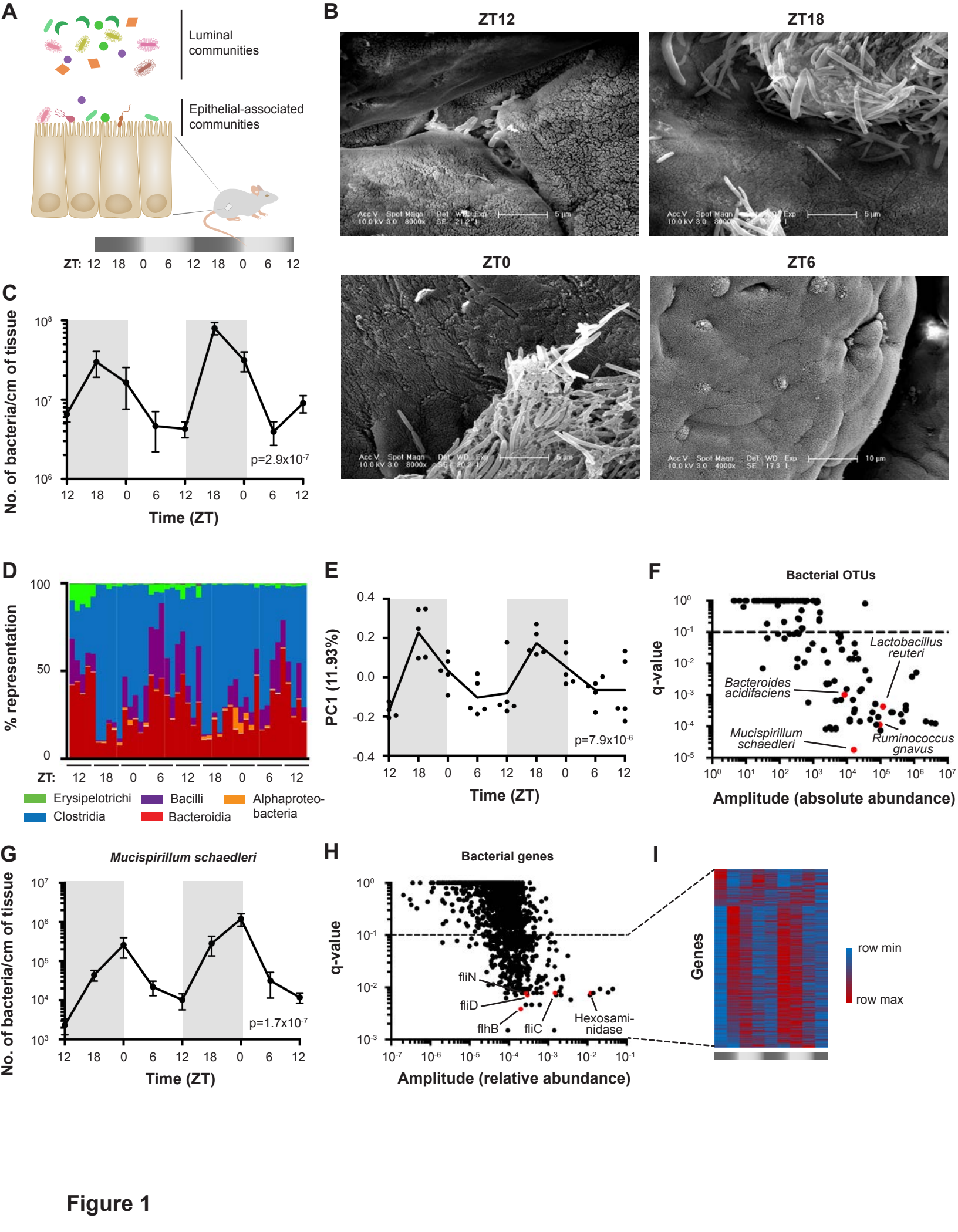
A
Luminal communities
Epithelial-associated communities
ZT: 12 18 0 6 12 18 0 6 12
B
ZT12
ZT18
ZT0
ZT6
C
No. of bacteria/cm of tissue
p=2.9x10-7
Time (ZT)
D
% representation
ZT: 12 18 0 6 12 18 0 6 12
Erysipelotrichi
Bacilli
Alphaproteo-bacteria
Clostridia
Bacteroidia
E
PC1 (11.93%)
p=7.9x10-6
Time (ZT)
F
Bacterial OTUs
q-value
Lactobacillus reuteri
Bacteroides acidifaciens
Mucispirillum schaedleri
Ruminococcus gnavus
Amplitude (absolute abundance)
G
Mucispirillum schaedleri
No. of bacteria/cm of tissue
p=1.7x10-7
Time (ZT)
H
Bacterial genes
q-value
fliN
fliD
flhB
fliC
Hexosami-nidase
Amplitude (relative abundance)
I
Genes
row min
row max

Figure 1

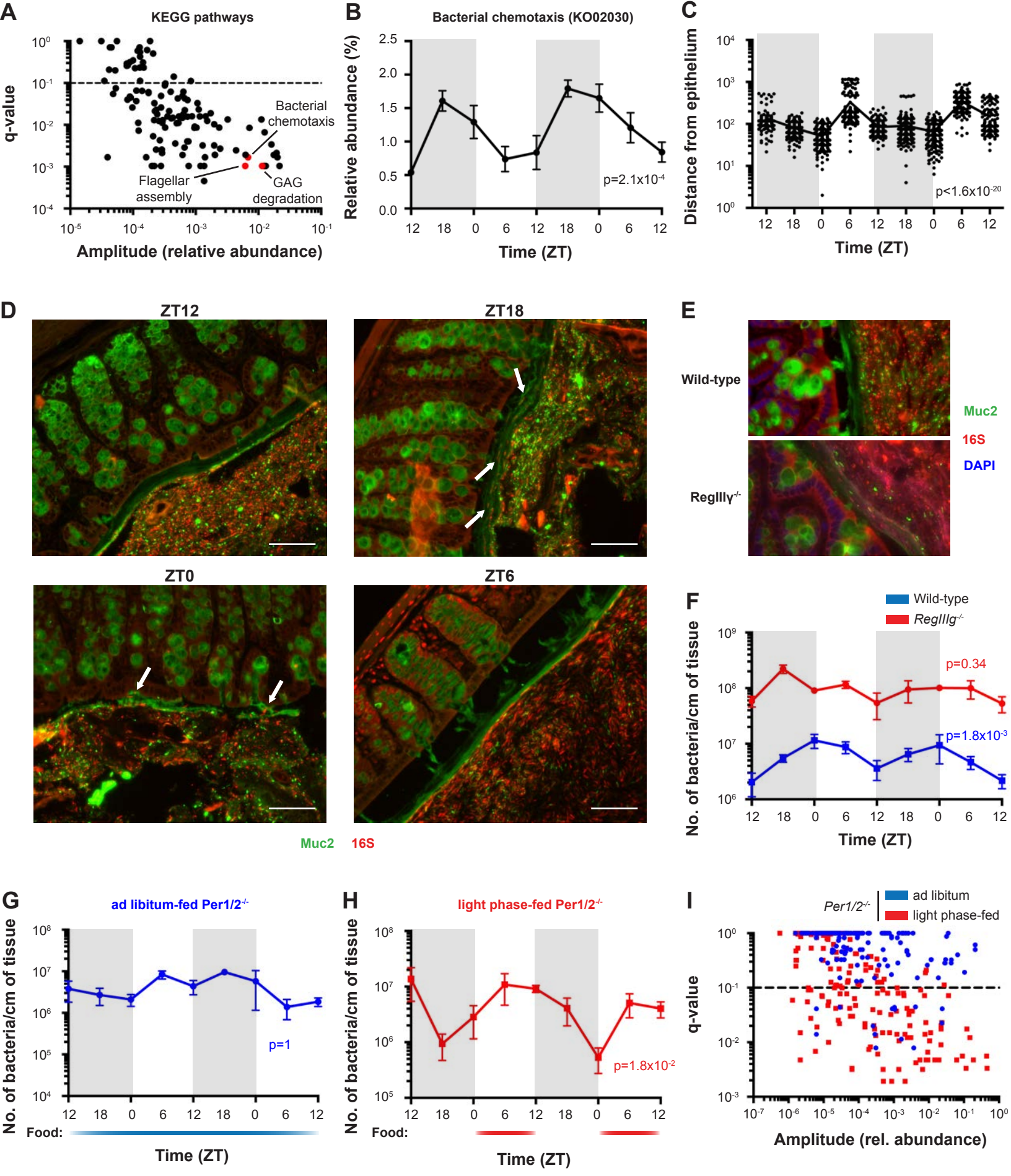
A
KEGG pathways
q-value
Bacterial chemotaxis
Flagellar assembly
GAG degradation
Amplitude (relative abundance)
B
Bacterial chemotaxis (KO02030)
Relative abundance (%)
p=2.1x10-4
Time (ZT)
C
Distance from epithelium
p<1.6x10-20
Time (ZT)
D
ZT12
ZT18
ZT0
ZT6
Muc2 16S
E
Wild-type
RegIIIγ-/-
Muc2
16S
DAPI
F
Wild-type
RegIIIg-/-
No. of bacteria/cm of tissue
p=0.34
p=1.8x10-3
Time (ZT)
G
ad libitum-fed Per1/2-/-
No. of bacteria/cm of tissue
p=1
Food:
Time (ZT)
H
light phase-fed Per1/2-/-
No. of bacteria/cm of tissue
p=1.8x10-2
Food:
Time (ZT)
I
Per1/2-/-
ad libitum
light phase-fed
q-value
Amplitude (rel. abundance)

Figure 2

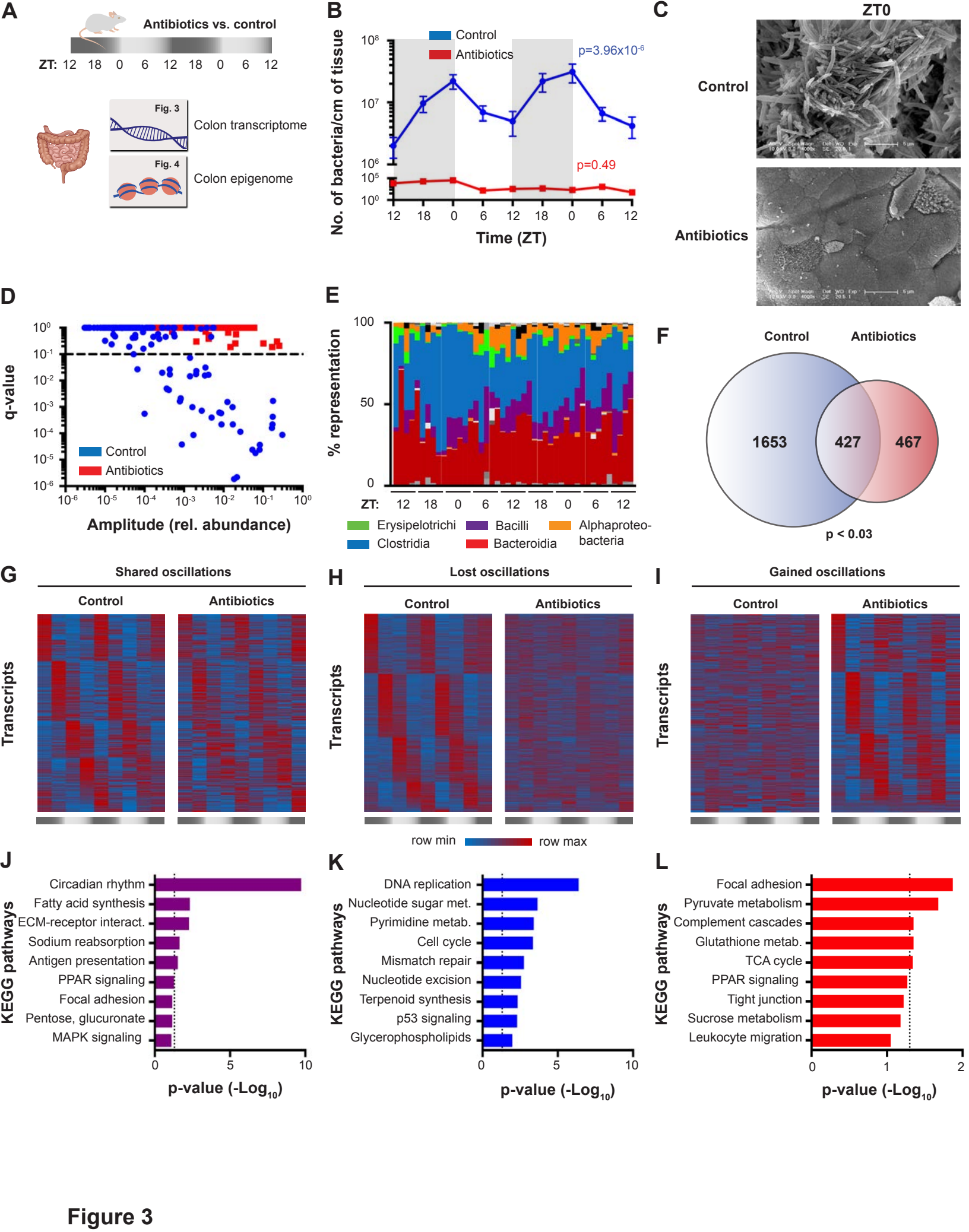
A
Antibiotics vs. control
ZT: 12 18 0 6 12 18 0 6 12
Fig. 3
Colon transcriptome
Fig. 4
Colon epigenome
B
Control
Antibiotics
p=3.96x10-6
p=0.49
No. of bacteria/cm of tissue
Time (ZT)
C
ZT0
Control
Antibiotics
D
q-value
Control
Antibiotics
Amplitude (rel. abundance)
E
% representation
ZT: 12 18 0 6 12 18 0 6 12
Erysipelotrichi
Bacilli
Alphaproteo-bacteria
Clostridia
Bacteroidia
F
Control
Antibiotics
1653
427
467
p < 0.03
G
Shared oscillations
Control
Antibiotics
Transcripts
H
Lost oscillations
Control
Antibiotics
Transcripts
I
Gained oscillations
Control
Antibiotics
Transcripts
row min
row max
J
KEGG pathways
Circadian rhythm
Fatty acid synthesis
ECM-receptor interact.
Sodium reabsorption
Antigen presentation
PPAR signaling
Focal adhesion
Pentose, glucuronate
MAPK signaling
p-value (-Log10)
K
KEGG pathways
DNA replication
Nucleotide sugar met.
Pyrimidine metab.
Cell cycle
Mismatch repair
Nucleotide excision
Terpenoid synthesis
p53 signaling
Glycerophospholipids
p-value (-Log10)
L
KEGG pathways
Focal adhesion
Pyruvate metabolism
Complement cascades
Glutathione metab.
TCA cycle
PPAR signaling
Tight junction
Sucrose metabolism
Leukocyte migration
p-value (-Log10)

Figure 3

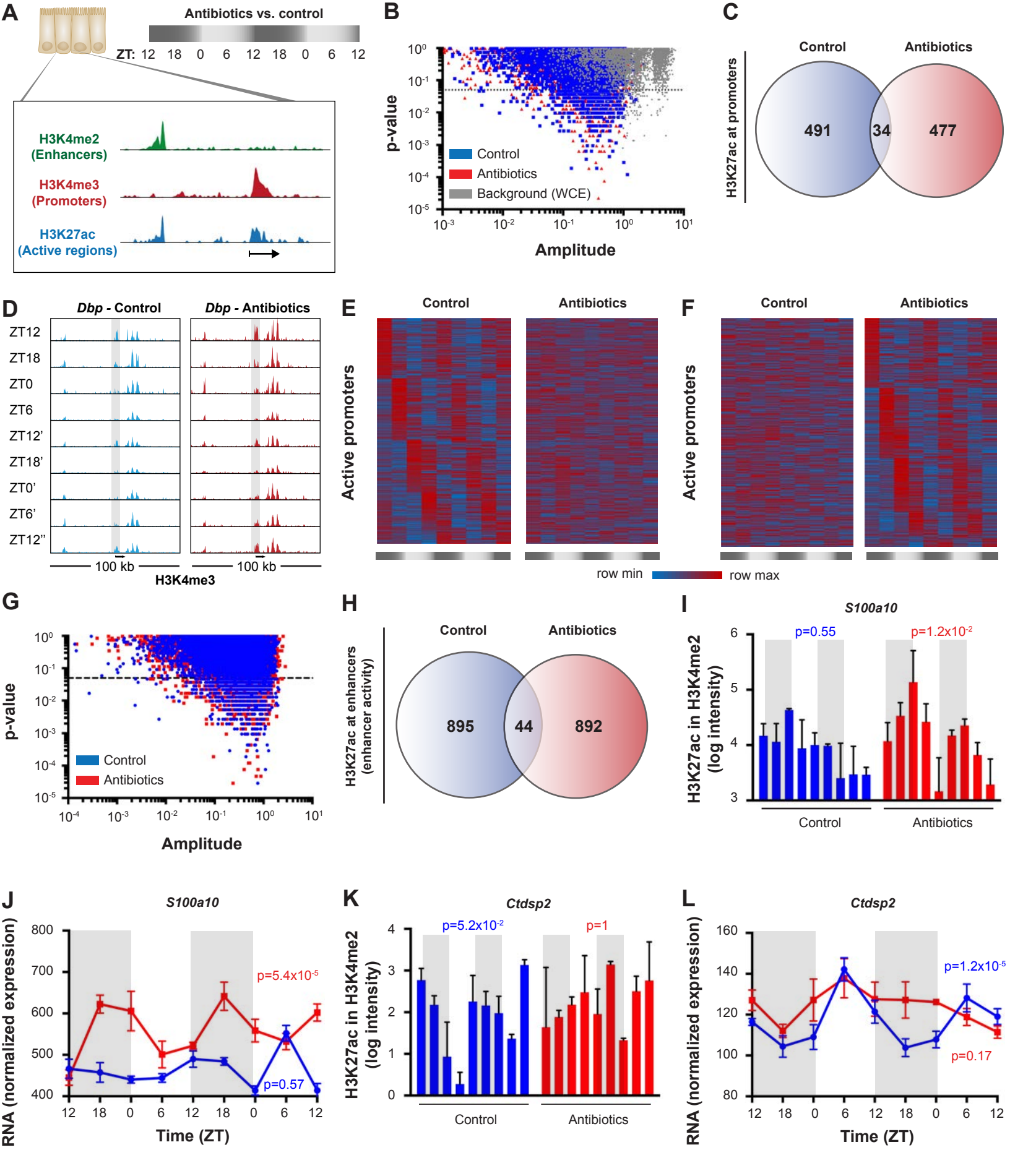
A
Antibiotics vs. control
ZT: 12 18 0 6 12 18 0 6 12
H3K4me2 (Enhancers)
H3K4me3 (Promoters)
H3K27ac (Active regions)
B
p-value
Control
Antibiotics
Background (WCE)
Amplitude
C
Control
Antibiotics
H3K27ac at promoters
491
34
477
D
Dbp - Control
Dbp - Antibiotics
ZT12
ZT18
ZT0
ZT6
ZT12'
ZT18'
ZT0'
ZT6'
ZT12''
100 kb
H3K4me3
E
Control
Antibiotics
Active promoters
F
Control
Antibiotics
Active promoters
row min
row max
G
p-value
Control
Antibiotics
Amplitude
H
Control
Antibiotics
H3K27ac at enhancers (enhancer activity)
895
44
892
I
S100a10
p=0.55
p=1.2x10-2
H3K27ac in H3K4me2 (log intensity)
Control
Antibiotics
J
S100a10
RNA (normalized expression)
p=5.4x10-5
p=0.57
Time (ZT)
K
Ctdsp2
p=5.2x10-2
p=1
H3K27ac in H3K4me2 (log intensity)
Control
Antibiotics
L
Ctdsp2
RNA (normalized expression)
p=1.2x10-5
p=0.17
Time (ZT)

Figure 4

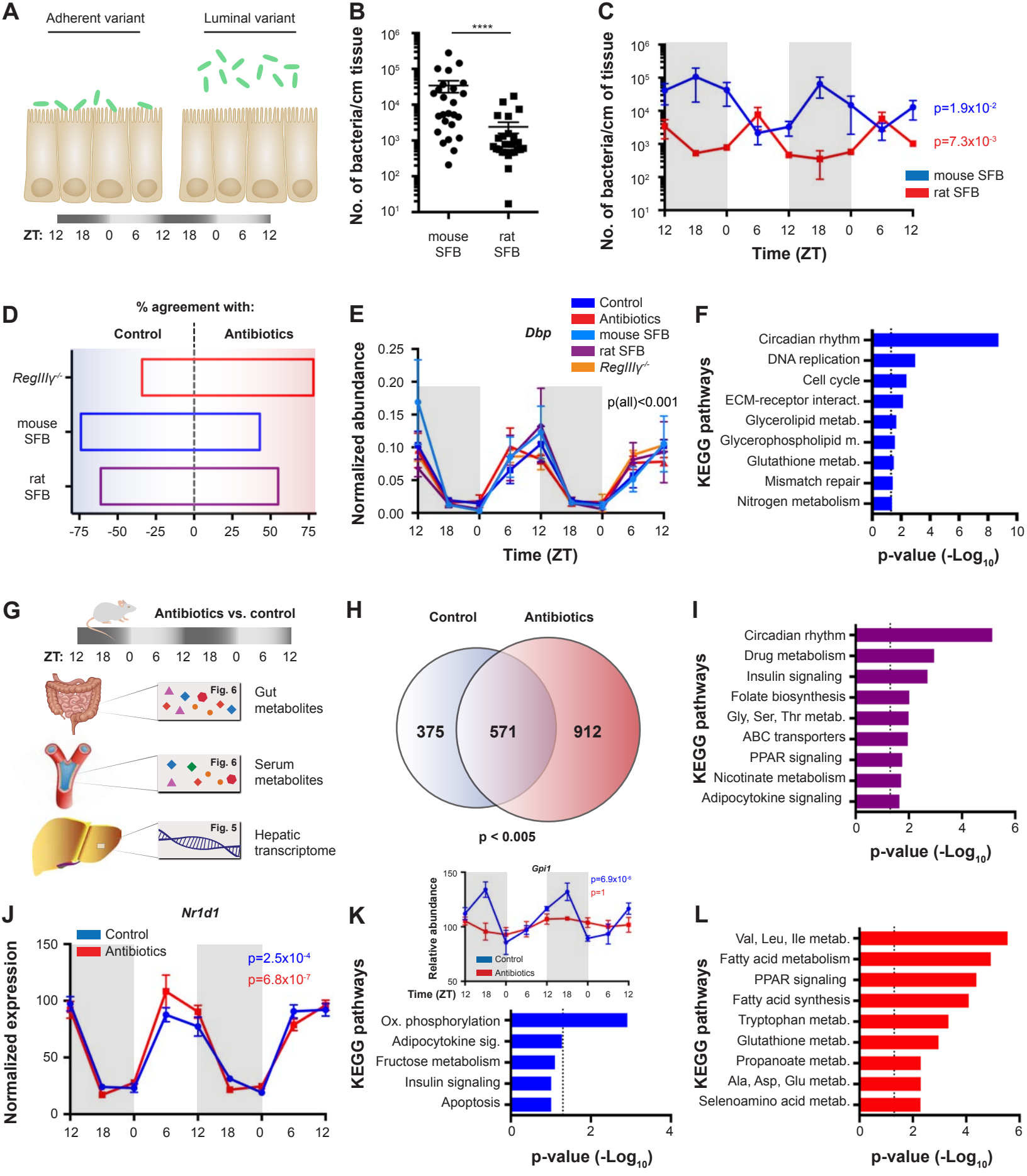
A
Adherent variant
Luminal variant
ZT: 12 18 0 6 12 18 0 6 12
B
No. of bacteria/cm tissue
****
mouse SFB
rat SFB
C
No. of bacteria/cm of tissue
p=1.9x10-2
p=7.3x10-3
mouse SFB
rat SFB
Time (ZT)
D
% agreement with:
Control
Antibiotics
RegIIIγ-/-
mouse SFB
rat SFB
E
Dbp
Control
Antibiotics
mouse SFB
rat SFB
RegIIIγ-/-
p(all)<0.001
Normalized abundance
Time (ZT)
F
KEGG pathways
Circadian rhythm
DNA replication
Cell cycle
ECM-receptor interact.
Glycerolipid metab.
Glycerophospholipid m.
Glutathione metab.
Mismatch repair
Nitrogen metabolism
p-value (-Log10)
G
Antibiotics vs. control
ZT: 12 18 0 6 12 18 0 6 12
Fig. 6
Gut metabolites
Fig. 6
Serum metabolites
Fig. 5
Hepatic transcriptome
H
Control
Antibiotics
375
571
912
p < 0.005
I
KEGG pathways
Circadian rhythm
Drug metabolism
Insulin signaling
Folate biosynthesis
Gly, Ser, Thr metab.
ABC transporters
PPAR signaling
Nicotinate metabolism
Adipocytokine signaling
p-value (-Log10)
J
Nr1d1
Control
Antibiotics
p=2.5x10-4
p=6.8x10-7
Normalized expression
K
Gpi1
p=6.9x10-6
p=1
Relative abundance
Control
Antibiotics
Time (ZT)
KEGG pathways
Ox. phosphorylation
Adipocytokine sig.
Fructose metabolism
Insulin signaling
Apoptosis
p-value (-Log10)
L
KEGG pathways
Val, Leu, Ile metab.
Fatty acid metabolism
PPAR signaling
Fatty acid synthesis
Tryptophan metab.
Glutathione metab.
Propanoate metab.
Ala, Asp, Glu metab.
Selenoamino acid metab.
p-value (-Log10)

Figure 5

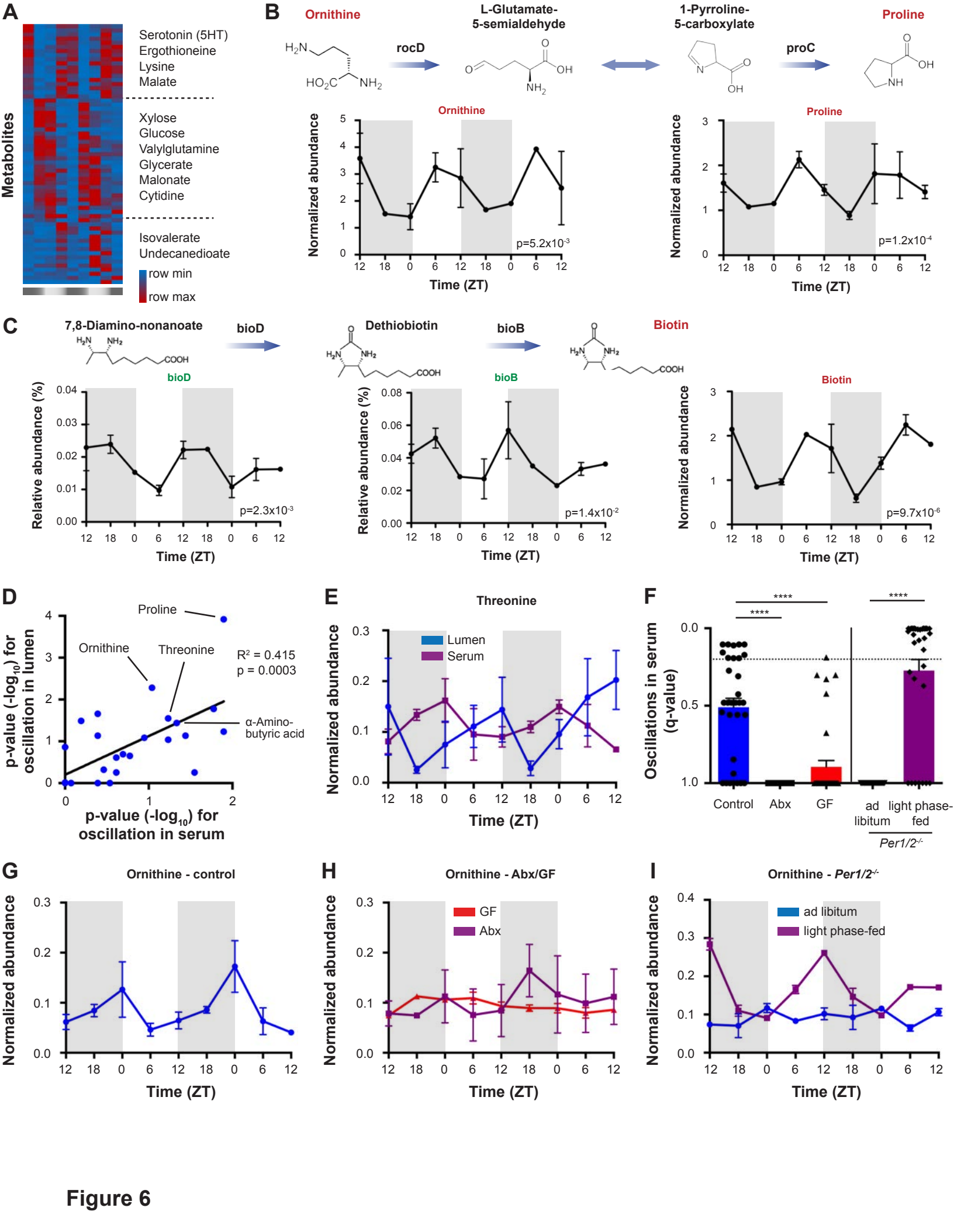
A
Metabolites
Serotonin (5HT)
Ergothioneine
Lysine
Malate
Xylose
Glucose
Valylglutamine
Glycerate
Malonate
Cytidine
Isovalerate
Undecanedioate
row min
row max
B
Ornithine
L-Glutamate-
5-semialdehyde
1-Pyrroline-
5-carboxylate
Proline
rocD
proC
Ornithine
Normalized abundance
p=5.2x10-3
Time (ZT)
Proline
p=1.2x10-4
C
7,8-Diamino-nonanoate
bioD
Dethiobiotin
bioB
Biotin
Relative abundance (%)
p=2.3x10-3
p=1.4x10-2
p=9.7x10-6
D
Proline
Ornithine
Threonine
R² = 0.415
p = 0.0003
α-Amino-
butyric acid
p-value (-log10) for
oscillation in lumen
p-value (-log10) for
oscillation in serum
E
Threonine
Lumen
Serum
F
Oscillations in serum
(q-value)
****
Control
Abx
GF
ad
libitum
light phase-
fed
Per1/2-/-
G
Ornithine - control
H
Ornithine - Abx/GF
GF
Abx
I
Ornithine - Per1/2-/-
ad libitum
light phase-fed
Time (ZT)

Figure 6

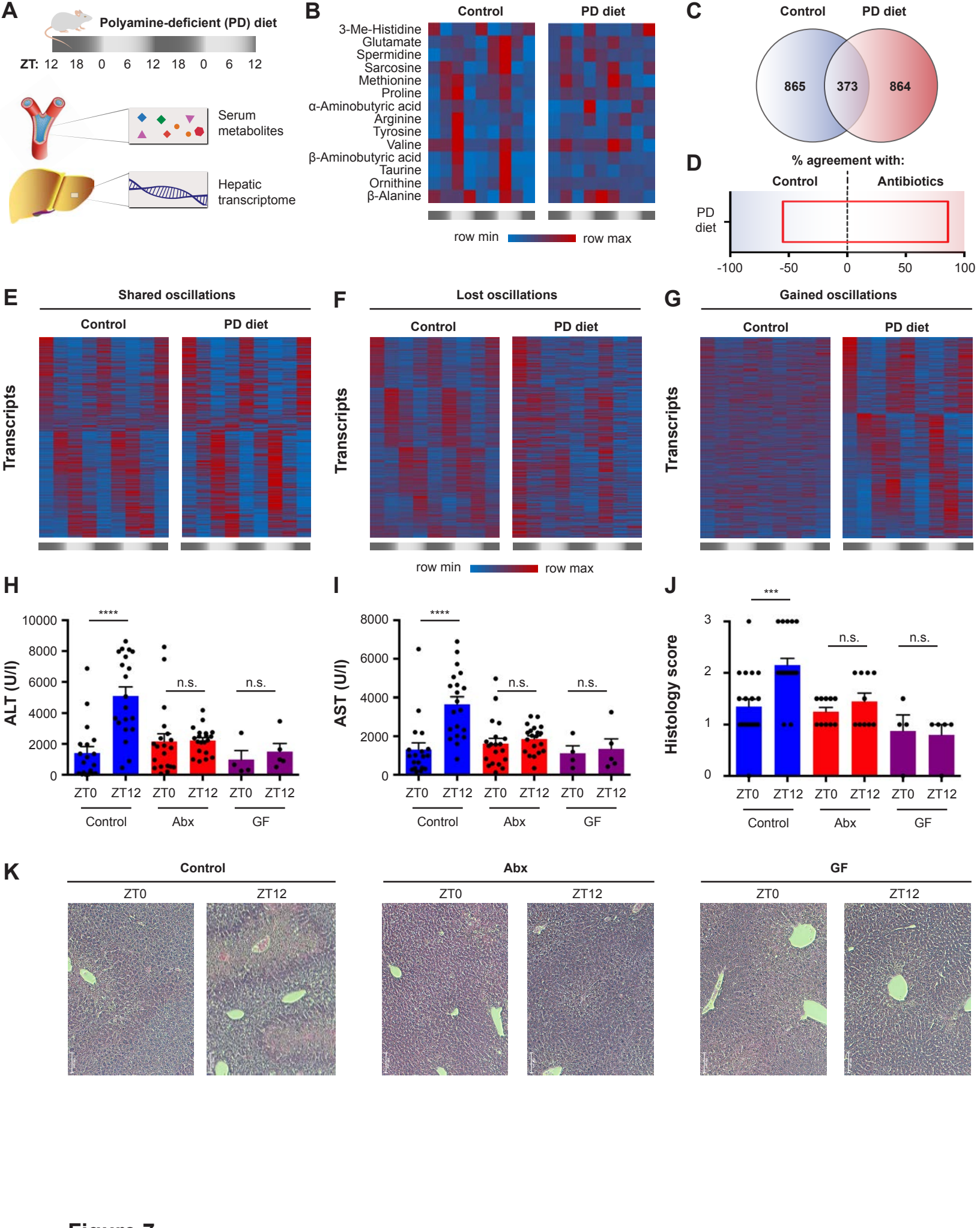
A
Polyamine-deficient (PD) diet
ZT: 12 18 0 6 12 18 0 6 12
Serum metabolites
Hepatic transcriptome
B
Control
PD diet
3-Me-Histidine
Glutamate
Spermidine
Sarcosine
Methionine
Proline
α-Aminobutyric acid
Arginine
Tyrosine
Valine
β-Aminobutyric acid
Taurine
Ornithine
β-Alanine
row min
row max
C
Control
PD diet
865
373
864
D
% agreement with:
Control
Antibiotics
PD diet
-100
-50
0
50
100
E
Shared oscillations
Control
PD diet
Transcripts
F
Lost oscillations
Control
PD diet
Transcripts
G
Gained oscillations
Control
PD diet
Transcripts
row min
row max
H
ALT (U/l)
10000
8000
6000
4000
2000
0
****
n.s.
n.s.
ZT0
ZT12
ZT0
ZT12
ZT0
ZT12
Control
Abx
GF
I
AST (U/l)
8000
6000
4000
2000
0
****
n.s.
n.s.
ZT0
ZT12
ZT0
ZT12
ZT0
ZT12
Control
Abx
GF
J
Histology score
3
2
1
0
***
n.s.
n.s.
ZT0
ZT12
ZT0
ZT12
ZT0
ZT12
Control
Abx
GF
K
Control
Abx
GF
ZT0
ZT12
ZT0
ZT12
ZT0
ZT12

Figure 7

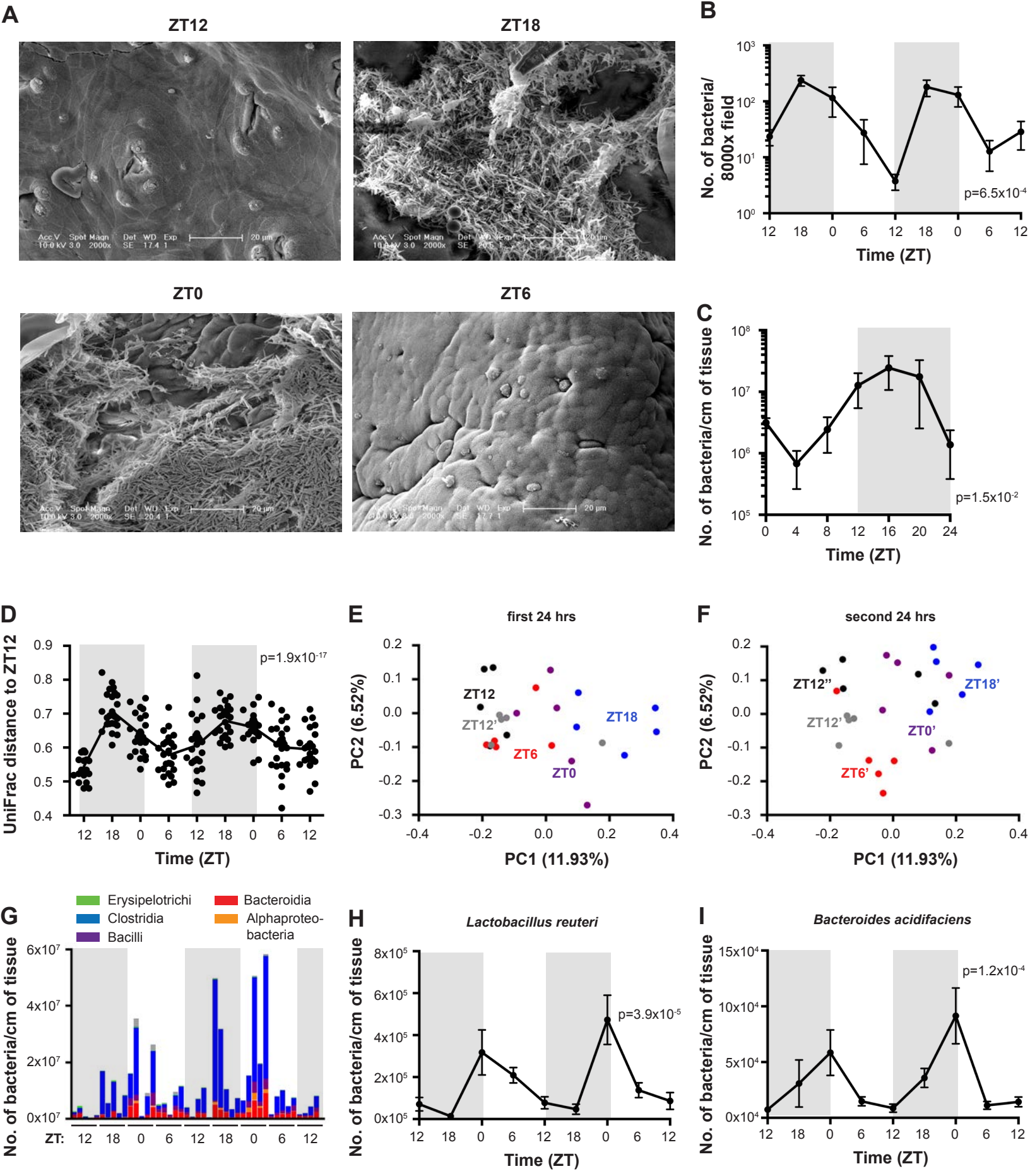
A
ZT12
ZT18
ZT0
ZT6
B
No. of bacteria/ 8000x field
p=6.5x10-4
Time (ZT)
C
No. of bacteria/cm of tissue
p=1.5x10-2
Time (ZT)
D
UniFrac distance to ZT12
p=1.9x10-17
Time (ZT)
E
first 24 hrs
PC2 (6.52%)
PC1 (11.93%)
ZT12
ZT12'
ZT18
ZT6
ZT0
F
second 24 hrs
PC2 (6.52%)
PC1 (11.93%)
ZT12''
ZT18'
ZT12'
ZT0'
ZT6'
G
Erysipelotrichi
Clostridia
Bacilli
Bacteroidia
Alphaproteo-bacteria
No. of bacteria/cm of tissue
ZT:
H
Lactobacillus reuteri
No. of bacteria/cm of tissue
p=3.9x10-5
Time (ZT)
I
Bacteroides acidifaciens
No. of bacteria/cm of tissue
p=1.2x10-4
Time (ZT)

Figure S1

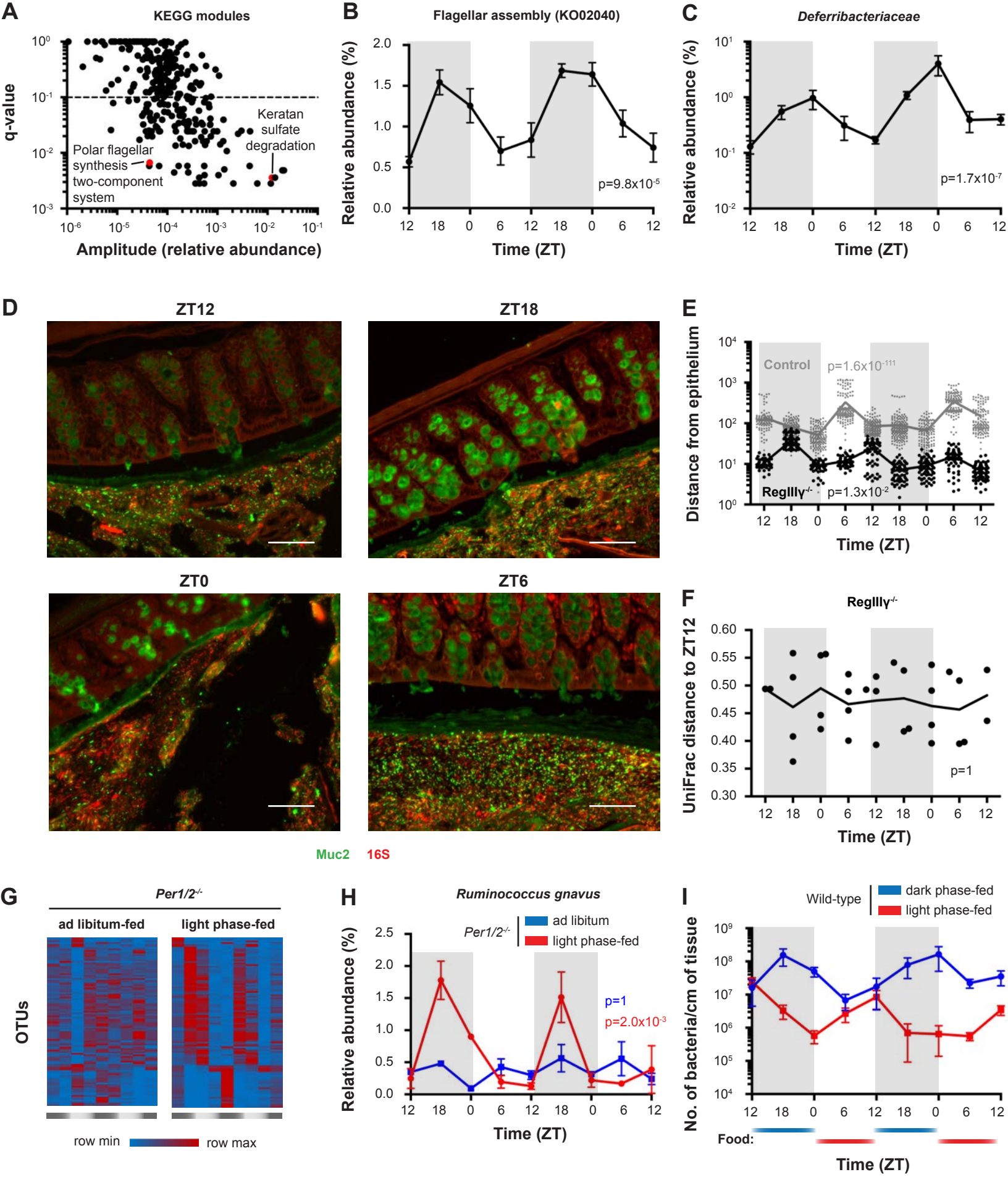
A
KEGG modules
q-value
Keratan sulfate degradation
Polar flagellar synthesis
two-component system
Amplitude (relative abundance)
B
Flagellar assembly (KO02040)
Relative abundance (%)
p=9.8x10-5
Time (ZT)
C
Deferribacteriaceae
Relative abundance (%)
p=1.7x10-7
Time (ZT)
D
ZT12
ZT18
ZT0
ZT6
Muc2
16S
E
Distance from epithelium
Control
p=1.6x10-111
Reglllγ-/-
p=1.3x10-2
Time (ZT)
F
Reglllγ-/-
UniFrac distance to ZT12
p=1
Time (ZT)
G
Per1/2-/-
ad libitum-fed
light phase-fed
OTUs
row min
row max
H
Ruminococcus gnavus
Per1/2-/-
ad libitum
light phase-fed
Relative abundance (%)
p=1
p=2.0x10-3
Time (ZT)
I
Wild-type
dark phase-fed
light phase-fed
No. of bacteria/cm of tissue
Food:
Time (ZT)

Figure S2

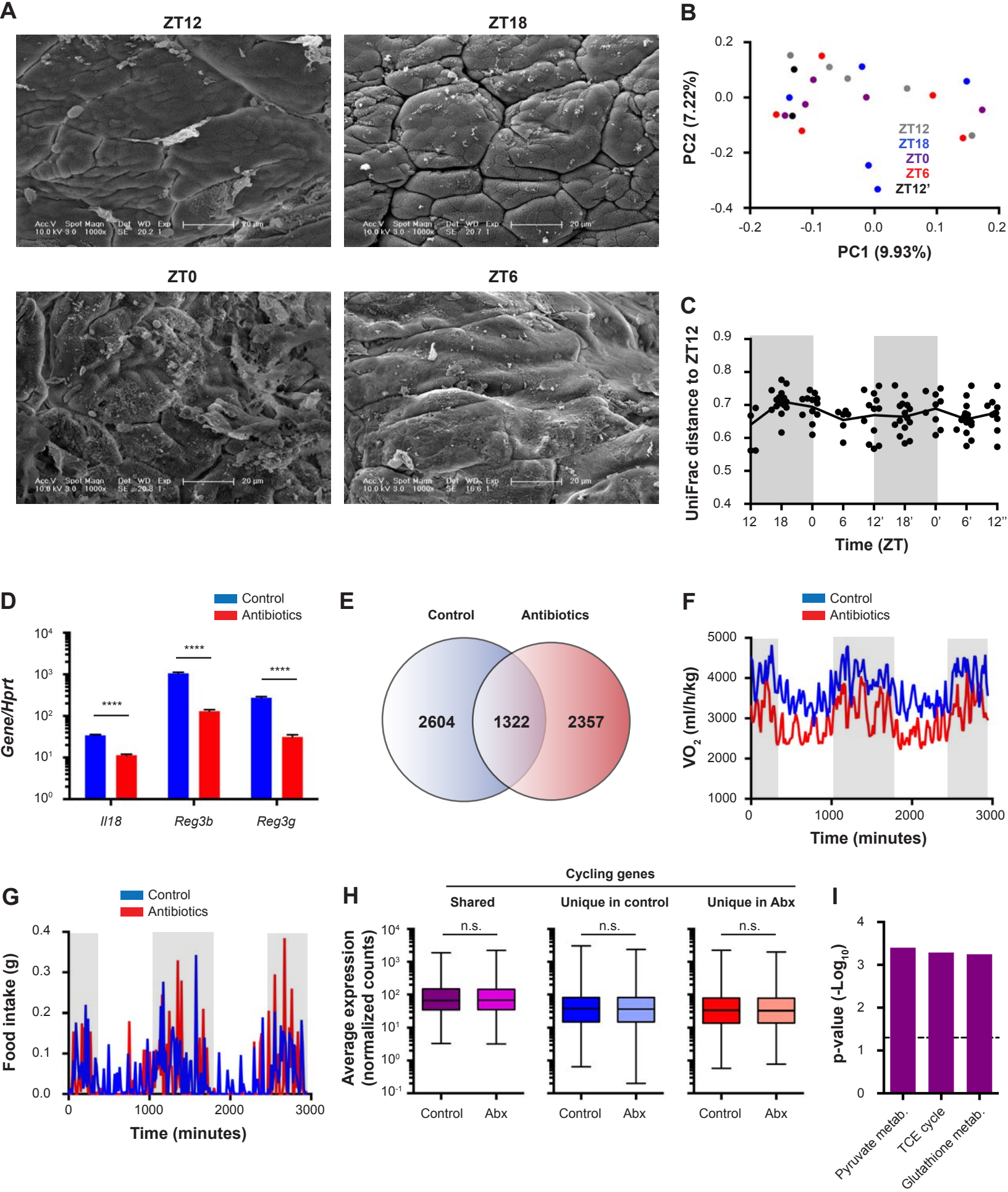
A
ZT12
ZT18
ZT0
ZT6
B
PC2 (7.22%)
PC1 (9.93%)
ZT12
ZT18
ZT0
ZT6
ZT12'
C
UniFrac distance to ZT12
Time (ZT)
12 18 0 6 12' 18' 0' 6' 12''
D
Control
Antibiotics
Gene/Hprt
Il18
Reg3b
Reg3g
****
E
Control
Antibiotics
2604
1322
2357
F
Control
Antibiotics
VO2 (ml/h/kg)
Time (minutes)
G
Control
Antibiotics
Food intake (g)
Time (minutes)
H
Cycling genes
Shared
Unique in control
Unique in Abx
Average expression (normalized counts)
n.s.
Control
Abx
I
p-value (-Log10)
Pyruvate metab.
TCE cycle
Glutathione metab.

Figure S3

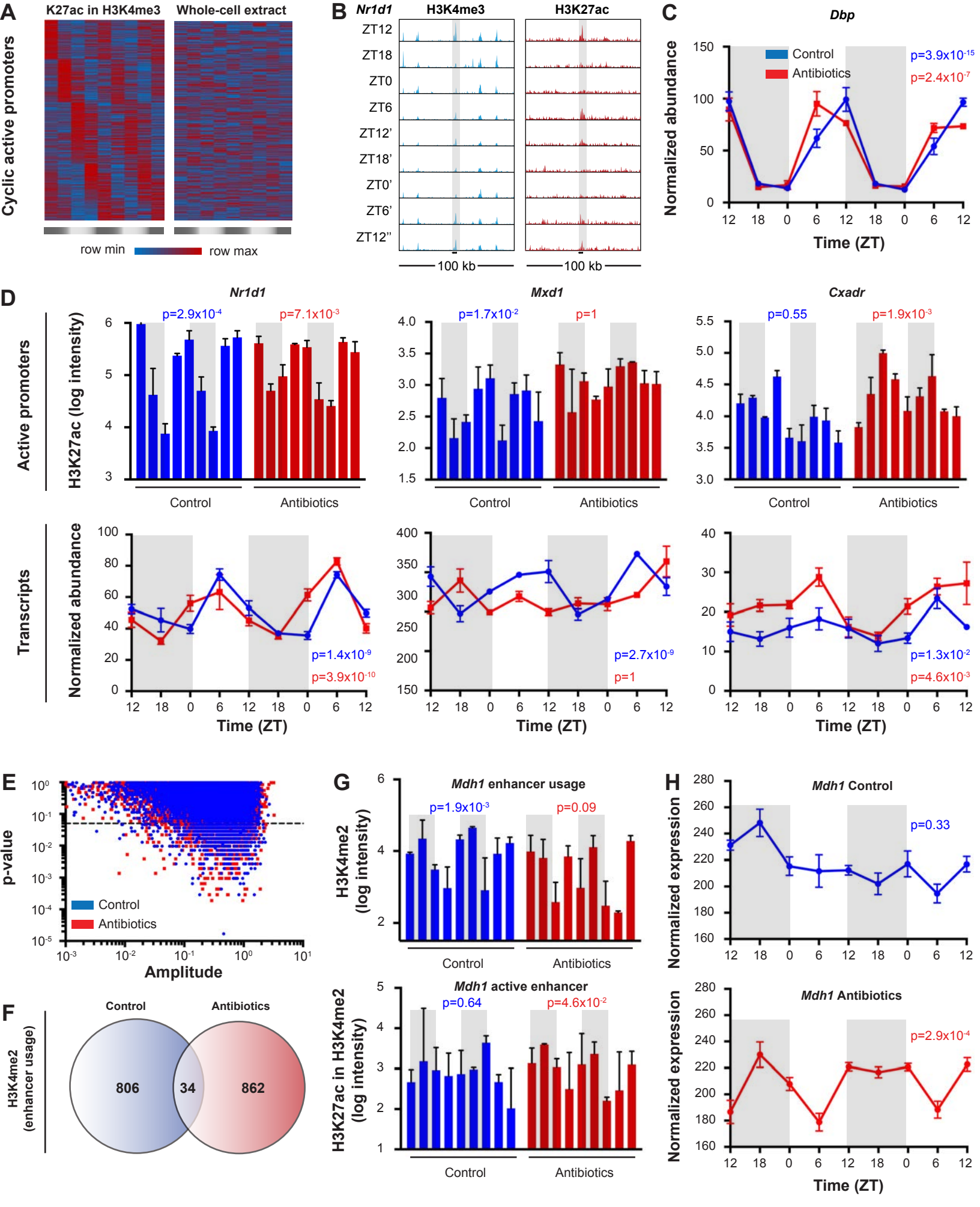
A
K27ac in H3K4me3
Whole-cell extract
Cyclic active promoters
row min
row max
B
Nr1d1
H3K4me3
H3K27ac
ZT12
ZT18
ZT0
ZT6
ZT12'
ZT18'
ZT0'
ZT6'
ZT12''
100 kb
100 kb
C
Dbp
Control
Antibiotics
p=3.9x10-15
p=2.4x10-7
Normalized abundance
Time (ZT)
D
Nr1d1
Mxd1
Cxadr
Active promoters
H3K27ac (log intensity)
p=2.9x10-4
p=7.1x10-3
p=1.7x10-2
p=1
p=0.55
p=1.9x10-3
Control
Antibiotics
Transcripts
Normalized abundance
p=1.4x10-9
p=3.9x10-10
p=2.7x10-9
p=1
p=1.3x10-2
p=4.6x10-3
Time (ZT)
E
p-value
Amplitude
Control
Antibiotics
F
H3K4me2 (enhancer usage)
Control
Antibiotics
806
34
862
G
Mdh1 enhancer usage
H3K4me2 (log intensity)
p=1.9x10-3
p=0.09
Control
Antibiotics
Mdh1 active enhancer
H3K27ac in H3K4me2 (log intensity)
p=0.64
p=4.6x10-2
Control
Antibiotics
H
Mdh1 Control
Normalized expression
p=0.33
Mdh1 Antibiotics
p=2.9x10-4
Time (ZT)

Figure S4

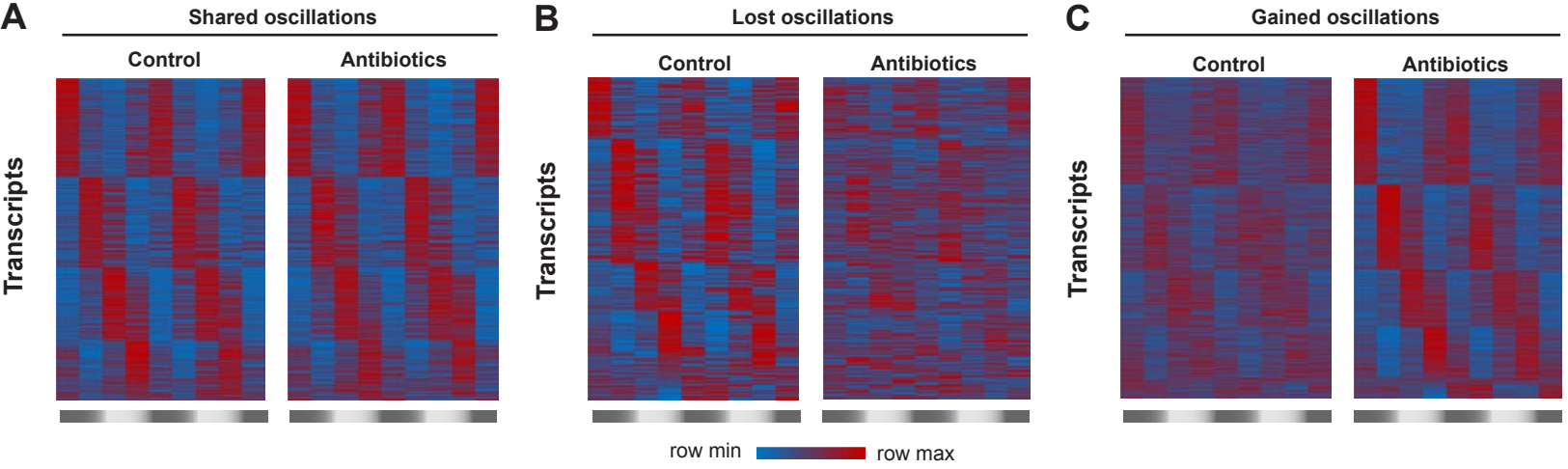
A
Shared oscillations
Control
Antibiotics
Transcripts
B
Lost oscillations
Control
Antibiotics
Transcripts
C
Gained oscillations
Control
Antibiotics
Transcripts
row min
row max

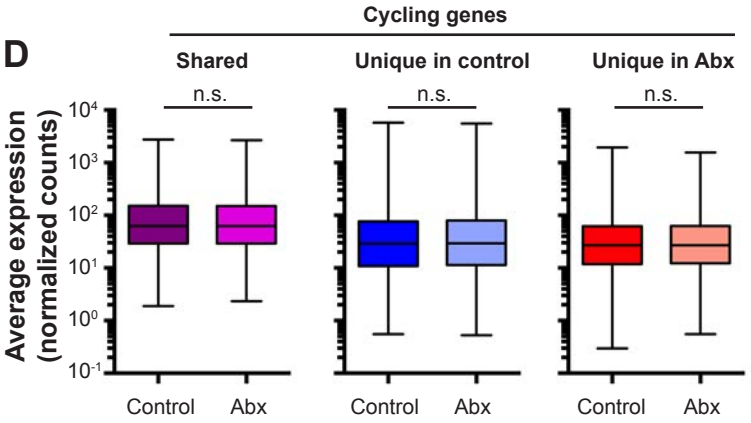
D
Cycling genes
Shared
Unique in control
Unique in Abx
n.s.
n.s.
n.s.
Average expression (normalized counts)
10^4
10^3
10^2
10^1
10^0
10^{-1}
Control
Abx
Control
Abx
Control
Abx

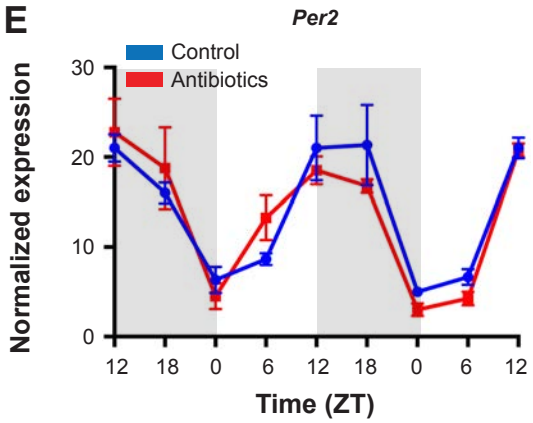
E
Per2
Control
Antibiotics
Normalized expression
30
20
10
0
12
18
0
6
12
18
0
6
12
Time (ZT)

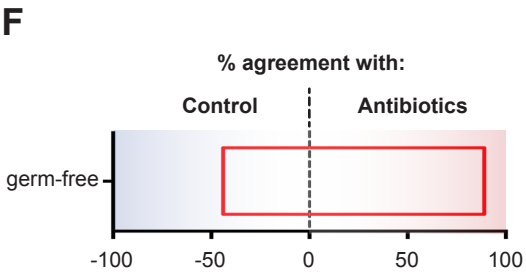
F
% agreement with:
Control
Antibiotics
germ-free
-100
-50
0
50
100

Figure S5

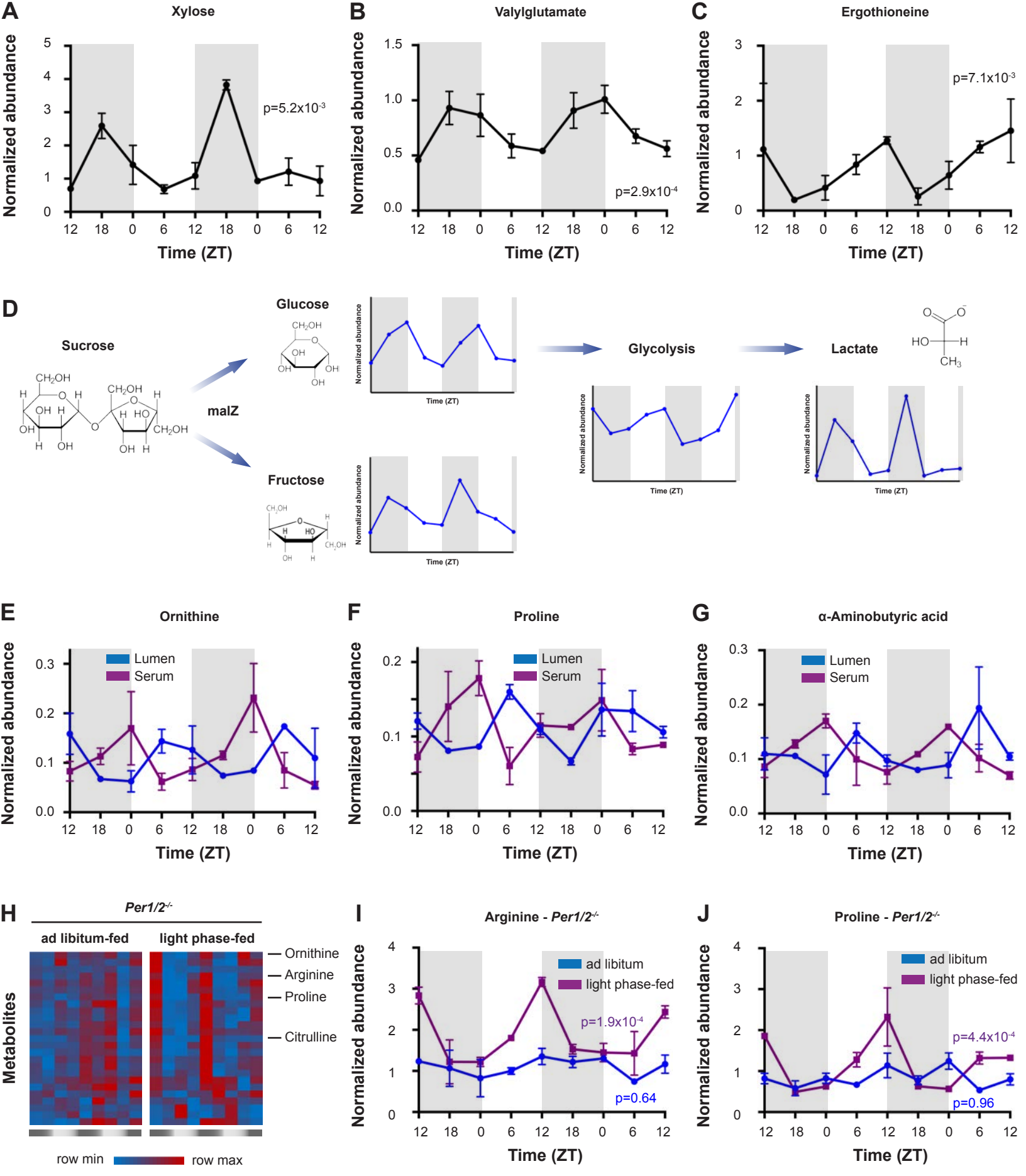
A
Xylose
Normalized abundance
p=5.2x10-3
Time (ZT)
B
Valylglutamate
p=2.9x10-4
C
Ergothioneine
p=7.1x10-3
D
Sucrose
malZ
Glucose
Fructose
Glycolysis
Lactate
E
Ornithine
Lumen
Serum
F
Proline
G
α-Aminobutyric acid
H
Per1/2-/-
ad libitum-fed
light phase-fed
Ornithine
Arginine
Proline
Citrulline
Metabolites
row min
row max
I
Arginine - Per1/2-/-
ad libitum
light phase-fed
p=1.9x10-4
p=0.64
J
Proline - Per1/2-/-
p=4.4x10-4
p=0.96

Figure S6

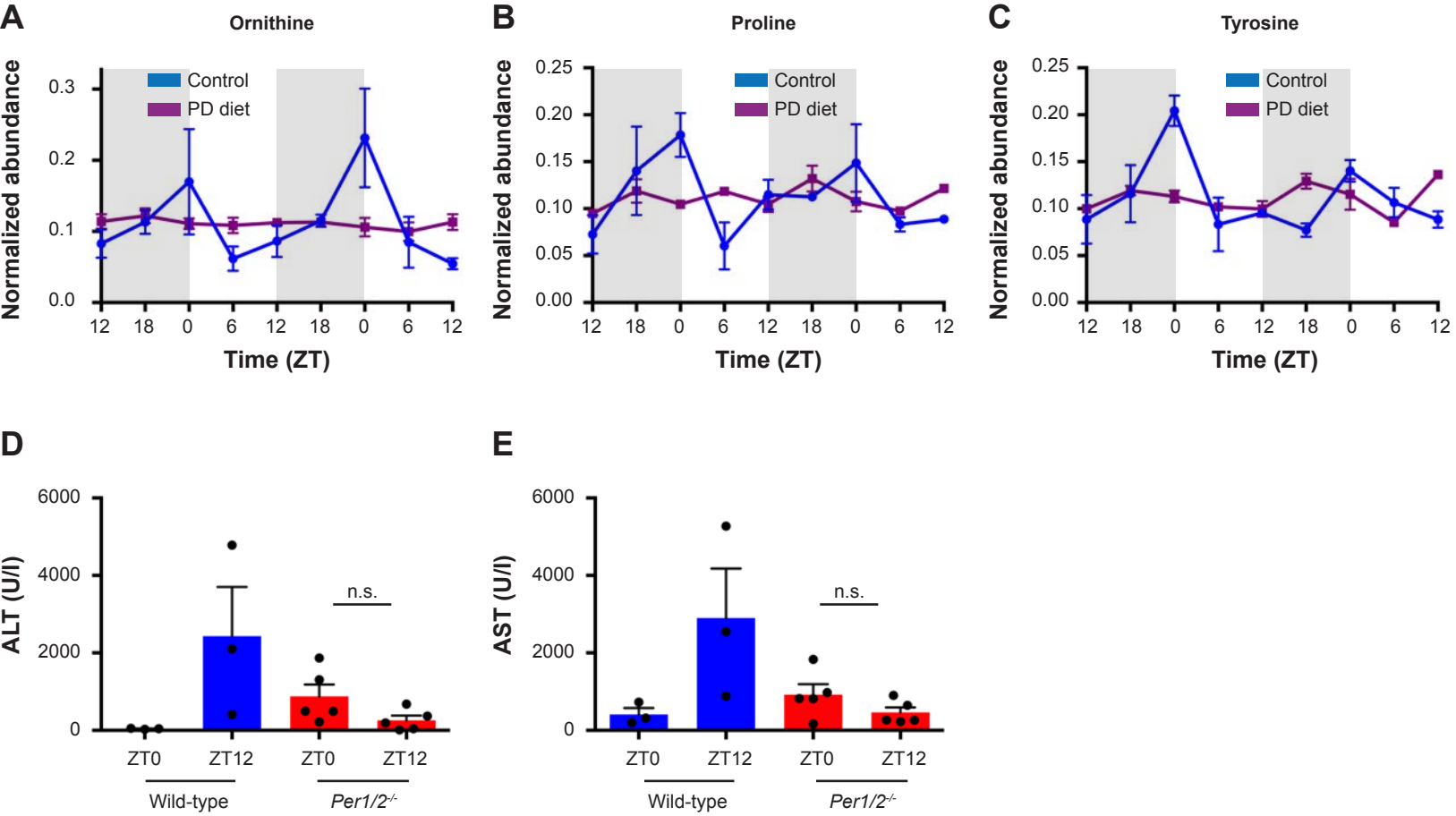
A
Ornithine
Normalized abundance
Control
PD diet
Time (ZT)
B
Proline
Normalized abundance
Control
PD diet
Time (ZT)
C
Tyrosine
Normalized abundance
Control
PD diet
Time (ZT)

D
ALT (U/l)
n.s.
ZT0
ZT12
ZT0
ZT12
Wild-type
Per1/2-/-
E
AST (U/l)
n.s.
ZT0
ZT12
ZT0
ZT12
Wild-type
Per1/2-/-

Figure S7

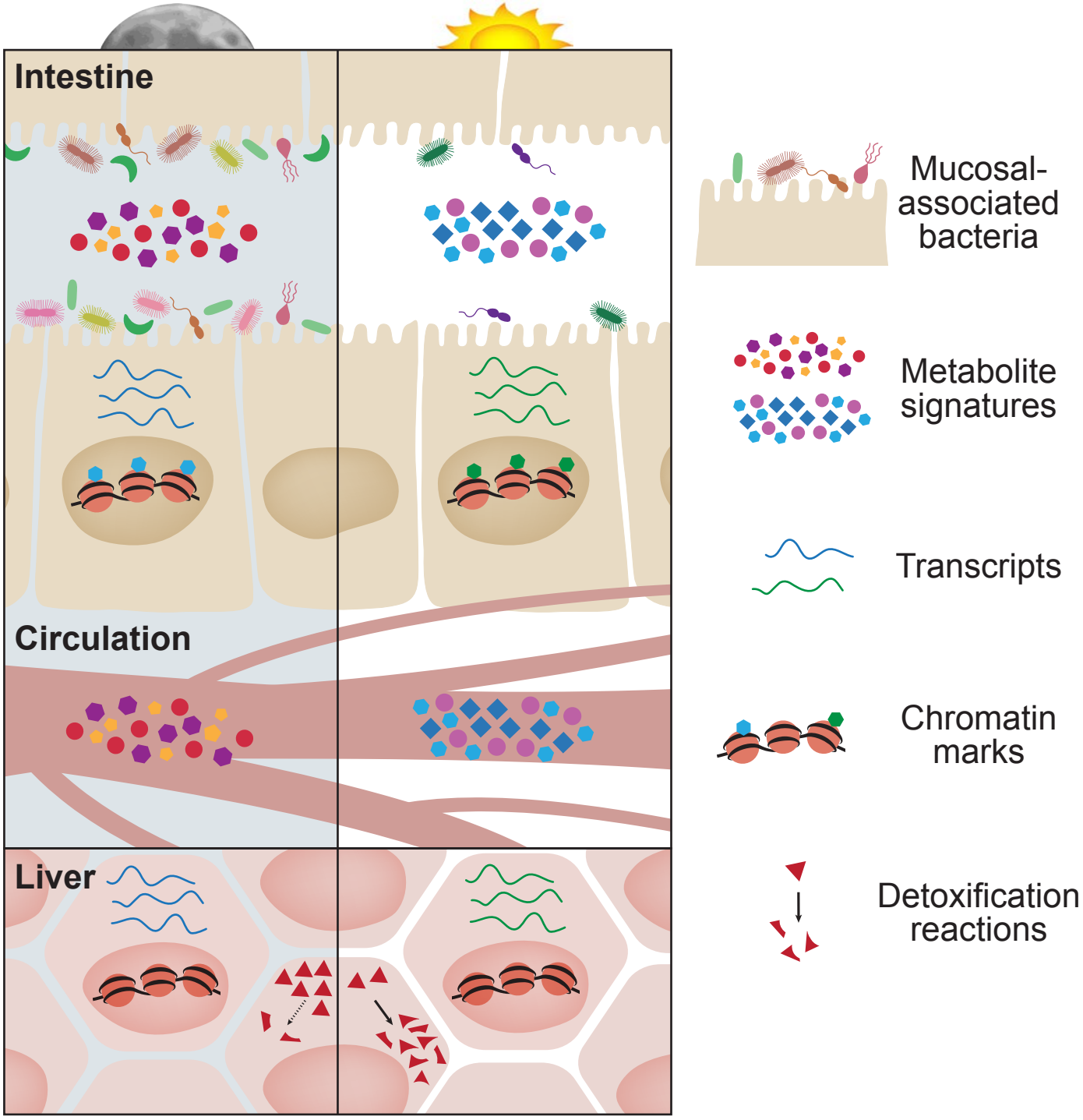

Graphical Abtract